

GREYSCALE - DENSITY CALIBRATION OF AN INDUSTRIAL CT SCANNER FOR WOOD MICRODENSITOMETRY

by

Marios Kadas



This thesis presented in fulfilment of the requirements for the degree of Master of Science in Forestry in the Faculty of Forest and Wood Science at Stellenbosch University

Supervisor: *Prof Thomas Seifert*

Co-supervisor: *Prof Martina Meincken*

March 2016

Declaration

By submitting this thesis/dissertation electronically, I declare that the entirety of the work contained therein is my own, original work, that I am the sole author thereof (save to the extent explicitly otherwise stated), that reproduction and publication thereof by Stellenbosch University will not infringe any third party rights and that I have not previously in its entirety or in part submitted it for obtaining any qualification.

March 2016

Abstract

The microdensitometry of wood, that is the quantification of density in the micrometre scale, is important for different scientific disciplines such as wood science, dendrochronology, dendroecology, dendroclimatology, and biomass determination and in the industrial applications of engineered wood. With the advent of industrial computed tomography scanners, powerful equipment for density measurement is available. However, the methodological framework for wood density determination with those machines is not fully established, because possible error sources have not so far been analysed and described sufficiently. Thus, the objective of this study was the development of a methodology, in order to quantify wood density with an industrial computed tomography scanner.

In this study, industrial cone-beam computed tomography was used for the microdensitometry of wood. Fifty stacks of stem discs from an equal number of *Pinus radiata* trees were used as the sample dataset. Firstly, the fifty stacks were scanned along with selected reference materials, which were measured for density in a conventional way. Then, fifty linear regressions were performed between the conventionally-determined density and the grey value of the reference materials. A strong correlation (mean $R^2=0.998$) between conventionally-determined density and grey value was observed. The regressions also provided calibration equations, which could translate a given grey value to a certain density. For validation purposes, the fifty calibration equations were tested on extra reference materials. The density from the computed tomography scanner had a mean absolute error of 0.008 g/cm^3 ($\sigma=0.004$) and a mean percent error of 1.4% ($\sigma=0.7$). Additionally, one of the calibration equations was applied to the creation of tree ring density profiles. An important result of the study was that it was not possible to deduce a sole calibration equation, as typically done with densitometers and medical computed tomography scanners. Thus, the calibration of each scan was inevitable, due to the various degrees of freedom of the industrial computed tomography scanner.

Opsomming

Die mikrodensitometrie van hout, dws die kwantifisering van die digtheid op die mikrometer skaal is belangrik vir verskillende wetenskaplike dissiplines soos houtwetenskap, dendro-chronologie, dendro-ekologie, dendro-klimatologie, biomassa bepaling en vir die industriële gebruik van verwerkte hout. Met die koms van die industriële tomografie skandeerders is kragtige toerusting vir die meting van houtdigtheid beskikbaar. Die metodologiese raamwerk vir die bepaling van hout digtheid met die masjiene is egter nog nie ten volle ontwikkel nie. Dit kan aanleiding gee tot metingsfoute wat nie voldoende geanaliseer en beskryf word nie. Die doel van hierdie studie is dus om 'n metode te ontwikkel om houtdigtheid te kwantifiseer deur die gebruik van 'n industriële tomografie-skandeerder.

In hierdie studie is industriële laser ligstraal tomografie gebruik om die mikrodensitometrie van hout te bepaal. Vir die monster datastel is vyftig stapels van die stam skywe van 'n gelyke aantal *Pinus radiata* bome gebruik. Eerstens is die vyftig stapels geskandeer saam met geselekteerde verwysingsmateriaal wat vir digtheid gemeet is op 'n konvensionele manier. Daarna is vyftig lineêre regressies ontwikkel tussen die digtheid wat bepaal is deur die konvensionele digtheidsmetode en die grys waarde van die verwysing materiaal. Met die studie is waargeneem dat daar 'n sterk korrelasie ($R^2 = 0.998$) is tussen die digtheid gemeet deur die gebruik van die konvensionele metode en die grys waarde. Die regressies voorsien ook kalibrasie vergelykings, wat 'n gegewe grys waarde kan assosieer met 'n sekere digtheid. Vir validerings doeleindes, is die vyftig kalibrasie vergelykings getoets op ekstra verwysingsmateriaal. Die digtheid gemeet deur die tomografie-skandeerder het 'n gemiddelde absolute afwyking van 0.008 g/cm^3 ($\sigma=0.004$) en 'n gemiddelde 1.4% ($\sigma=0.7$) fout getoon. Verder is een van die ontwikkelde kalibrasie vergelykings toegepas om boomring digtheidsprofile te skep. Die studie het bevind dat 'n enkele kalibrasie vergelyking nie gebruik kan word soos tipies met die gebruik van densitometers en mediese tomografie skandeerders nie. Die industriële tomografie-skandeerder moes dus gekalibreer word met elke skandering as gevolg van die verskillende grade van vryheid wat bevind is in die studie.

Σύνοψη

Η μικροπυκνομετρία του ξύλου, δηλαδή η ποσοτικοποίηση της πυκνότητας στην κλίμακα του μικρομέτρου, είναι σημαντική για διάφορα επιστημονικά πεδία όπως η επιστήμη του ξύλου, η δένδροχρονολογία, η δένδροοικολογία, η δένδροκλιματολογία, και ο καθορισμός της βιομάζας και σε βιομηχανικές εφαρμογές επεξεργασμένου ξύλου. Με την άφιξη των βιομηχανικών υπολογιστικών τομογράφων, ισχυρός εξοπλισμός για τη μέτρηση της πυκνότητας είναι διαθέσιμος. Παρ' όλα αυτά, το μεθοδολογικό πλαίσιο για τον καθορισμό της πυκνότητας του ξύλου με αυτά τα μηχανήματα δεν είναι πλήρως εδραιωμένο, επειδή πιθανές πηγές σφάλματος δεν έχουν μέχρι στιγμής αναλυθεί και περιγραφεί επαρκώς. Συνεπώς, το αντικείμενο αυτής της μελέτης ήταν η ανάπτυξη μιας μεθοδολογίας, ώστε να ποσοτικοποιηθεί η πυκνότητα του ξύλου με ένα βιομηχανικό υπολογιστικό τομογράφο.

Σε αυτήν τη μελέτη, η βιομηχανική υπολογιστική τομογραφία κωνικής δέσμης χρησιμοποιήθηκε για τη μικροπυκνομετρία του ξύλου. Πενήντα στοίβες δίσκων κορμών από ένα ίσο αριθμό δέντρων *Pinus radiata* χρησιμοποιήθηκαν ως δείγμα δεδομένων. Αρχικά, οι πενήντα στοίβες σκαναρίστηκαν μαζί με επιλεγμένα υλικά αναφοράς, στα οποία μετρήθηκε η πυκνότητα με συμβατικό τρόπο. Μετά, πενήντα γραμμικές παλινδρομήσεις έγιναν μεταξύ της συμβατικά-καθορισμένης πυκνότητας και της τιμής του γκρι των υλικών αναφοράς. Παρατηρήθηκε μια ισχυρή συσχέτιση (μέσος όρος των $R^2=0.998$) μεταξύ της συμβατικά-καθορισμένης πυκνότητας και της τιμής του γκρι. Οι παλινδρομήσεις επίσης παρείχαν εξισώσεις καλιμπραρίσματος, οι οποίες μπορούσαν να μεταφράσουν μια δοθείσα τιμή του γκρι σε μια συγκεκριμένη πυκνότητα. Για λόγους επαλήθευσης, οι πενήντα εξισώσεις καλιμπραρίσματος δοκιμάστηκαν σε έξτρα υλικά αναφοράς. Η πυκνότητα από τον υπολογιστικό τομογράφο είχε μέσο απόλυτο σφάλμα 0.008 g/cm^3 ($\sigma=0.004$) και μέσο τοις εκατό σφάλμα 1.4% ($\sigma=0.7$). Επιπροσθέτως, μία από τις εξισώσεις καλιμπραρίσματος εφαρμόστηκε στην δημιουργία προφίλ πυκνότητας δακτυλίων δέντρων. Ένα σημαντικό αποτέλεσμα της μελέτης ήταν ότι δεν ήταν δυνατόν να χρησιμοποιηθεί μια μοναδική εξίσωση καλιμπραρίσματος, όπως τυπικά γίνεται με τους πυκνομετρητές και τους ιατρικούς υπολογιστικούς τομογράφους. Συνεπώς, το καλιμπράρισμα του κάθε σκαναρίσματος ήταν αναπόφευκτο, εξαιτίας των διαφόρων βαθμών ελευθερίας του βιομηχανικού υπολογιστικού τομογράφου.

Acknowledgements

I would like to acknowledge:

Prof Thomas Seifert for his unique guidance throughout the project.

Dr Anton du Plessis for his great amount of personal contribution to the design and the realization of the CT scanner experiments.

Dr Martina Meincken for her useful advice.

Mr Mark February, Mr Wilmour Hendrikse, and Mr Yos Weerdenburg for the cut of the imaging phantom.

Mr Otto Pienaar for the translation of the abstract.

Mr Phillip Fischer for the *P. radiata* samples.

Ms Angeline Atsame-Edda, Ms Dorothea van Vuuren, Mr Emile Kitenge, Mr Robert Mupemba, Dr Benedict Ohdiambo and Ms Ursula Petersen for their great help with the project.

NRF/BMBF-project FORSIM and the EU Marie Curie IRSEs project: "Climate Fit Forests" for the financial support for sampling and CT scanning.

Table of Contents

List of Tables	iii
List of Figures	iv
List of Equations	v
List of Abbreviations	vi
1. Introduction.....	1
1.1. X-ray computed tomography	1
1.1.1. Principle of operation	1
1.1.2. Linear attenuation coefficient	2
1.1.3. CT numbers	3
1.2. CT densitometry	3
1.3. Motivation	4
1.4. Identification of gaps of knowledge.....	5
2. Materials and Methods	7
2.1. Overall objective	7
2.2. Summary of the methodology.....	7
2.3. Imaging phantom and wood samples	9
2.4. CT scanning procedure	11
2.5. Greyscale - density calibration.....	16
2.6. Tree ring CT density profile	20
2.7. Potential sources of CT density error.....	23
2.7.1. Homogeneity of phantom slices	23
2.7.2. Number of phantom slices.....	23
3. Results.....	24
3.1. Greyscale - density calibration.....	24
3.2. Tree ring CT density profile	29

3.3. Potential sources of CT density error.....	32
3.3.1. Homogeneity of phantom slices	32
3.3.2. Number of phantom slices.....	32
4. Discussion	33
4.1. Accuracy and repeatability of the greyscale - density calibration.....	33
4.1.1. CT density error	33
4.1.2. Homogeneity of phantom slices	33
4.1.3. Number of phantom slices.....	34
4.1.4. Chemical composition of phantom slices	34
4.1.5. Stability of the calibrations.....	35
4.2. Spatial accuracy	35
4.3. Outlook on future work.....	36
5. Conclusions	38
6. Reference List	39
Appendix A. Regression example.....	47
Appendix B. Regression results.....	48

List of Tables

Table 1 - The minimum, maximum and average diameter of the discs of each height	11
Table 2 - The settings of the scans	12
Table 3 - Example of a CT density profile table	21
Table 4 - Air-dry conventionally-determined density of the phantom slices	24
Table 5 - The mean CT density of each stem disc	29
Table 6 - Example of a regression dataset	47
Table 7 - The equations and the coefficients of determination of the regressions	48

List of Figures

Figure 1 - The configuration of an industrial cone beam CT scanner	1
Figure 2 - A synopsis of the methodology	8
Figure 3 - The imaging phantom	10
Figure 4 - A part of the Pinus radiata stacks which were used for testing the method	10
Figure 5 - An X-ray image from a CT scan	13
Figure 6 - A reconstructed volume	14
Figure 7 - A cross-section of a reconstructed volume	15
Figure 8 - A cross-sectional image with pseudocolour	17
Figure 9 - CT density profile selection on Image J	21
Figure 10, 11 and 12 - The effect of the strip width (1, 10, and 25 pixels) on the density profile	22
Figure 13 - One of the fifty greyscale - density regressions	25
Figure 14 - The dispersion of the calibration equations	26
Figure 15 - The frequency of reconstructed volumes per CT density error	28
Figure 16 - The frequency of reconstructed volumes per CT density error (%)	28
Figure 17 - The CT density profile of stem disc 1	29
Figure 18 - The CT density profile of stem disc 2	30
Figure 19 - The CT density profile of stem disc 3	30
Figure 20 - The CT density profile of stem disc 4	31
Figure 21 - The CT density profile of stem disc 5	31
Figure 22 - The confidence intervals of regressions with 4, 6, 8, 10, and 12 materials	32

List of Equations

Equation 1 - The total linear attenuation coefficient	2
Equation 2 - The measured intensity of monochromatic radiation penetrating a homogeneous material	3
Equation 3 - Translation of a grey value into CT density	18
Equation 4 - The absolute error of the CT density of a phantom slice	19
Equation 5 - The percent error of the CT density of a phantom slice	19

List of Abbreviations

CT	Computed tomography
gv	Grey value
μ	Linear attenuation coefficient
ρ_C	Density determined by conventional methods e.g. calliper and scale, water displacement
ρ_{CT}	Density determined by a CT scanner
σ	Standard deviation of a population

1. Introduction

1.1. X-ray computed tomography

1.1.1. Principle of operation

Computed tomography (CT) is a non-invasive method that provides the ability to study the internal space of an object and to make distance, volume, and density measurements (Kalender, 2000).

X-ray CT scanners achieve this by acquiring a series of perimetrical X-ray images of an object (Figure 1). The value of a pixel of an X-ray image is the value of the linear attenuation coefficient (μ) of the X-ray beam on the way through the scanned object. It can be visualized as a grey value (gv) (Lindgren 1991a, Kalender, 2000). Then, an algorithmic process of reconstruction (typically filtered back projection) is used for creating a three-dimensional voxel-based volume by using the linear attenuation coefficient of the perimetrical X-ray images (Kalender, 2000).



Figure 1 - The configuration of an industrial cone beam CT scanner

The scanned object is rotated in order to provide a series of perimetrical X-ray images. The position of the X-ray detector and the rotator can be customized in relation to the X-ray tube.

1.1.2. Linear attenuation coefficient

During a CT scan, an amount of X-ray photons will penetrate a material and the rest will interact with it depending on the properties of the X-rays and the atoms. The significant interaction events are the Compton scattering and the photoelectric absorption, while events which are either insignificant or observed under extreme conditions are elastic scattering, photodisintegration, and pair production. Therefore, the attenuation of X-ray photons by a certain material is expressed with the linear attenuation coefficient which is the sum of the attenuation coefficients that result from the Compton scattering and from the photoelectric absorption (Equation 1) (Mull, 1984; Lindgren, 1991a, 1991b; Phillips & Lannutti, 1997).

$$\mu = \mu_c(\rho, E) + \mu_p(\rho, E, Z)$$

Equation 1 - The total linear attenuation coefficient

μ : The total linear attenuation coefficient

μ_c : The attenuation coefficient that results from the Compton scattering

μ_p : The attenuation coefficient that results from the photoelectric absorption

ρ : The density of the material

E : The energy of the photon

Z : The effective atomic number of the material

According to Beer-Lambert law, the linear attenuation coefficient of monochromatic radiation penetrating a chemically homogeneous material can be calculated based on the initial and measured intensity of the X-rays and the material's thickness (Equation 2) (Beer, 1852; Hoag, 1988; Phillips & Lannutti, 1997; Kalender, 2000; Nikolova et al., 2009, Seifert et al. 2010). However, for a CT scanner that is used to scan an inhomogeneous material with polychromatic radiation, the linear attenuation coefficient will be a function of energy and position (Kalender, 2000).

$$I = I_0 e^{-\mu d}$$

Equation 2 - The measured intensity of monochromatic radiation penetrating a homogeneous material

I: Measured intensity

*I*₀: Initial intensity

e: Euler's constant (≈2.718)

μ: Linear attenuation coefficient

d: Material thickness

1.1.3. CT numbers

Thus, a measured linear attenuation coefficient cannot be compared with a linear attenuation coefficient from a different material, scan or scanner (Kalender, 2000). For this reason, the medical CT scanners typically rescale the linear attenuation coefficient to normalized radiodensity values. The radiodensity scale of CT numbers or Hounsfield Units (HU) assigns the linear attenuation coefficient of water to 0 HU and the linear attenuation coefficient of air to -1000 HU (Kalender, 2000; Hou et al., 2007).

1.2. CT densitometry

The densitometry of variations in wood samples, such as tree ring cores or panels, with the conventional method (volume divided by weight) is a time-consuming and destructive process. In literature, fast and non-destructive wood densitometric methods beyond X-ray imaging include:

- (i) High-frequency microscopy (Schinker et al., 2003)
- (ii) Magnetic resonance imaging (Bucur, 2003a)
- (iii) Microwave imaging (Bucur, 2003a)
- (iv) Neutron imaging (De Ridder et al., 2011)
- (v) Optical microscopy (Decoux et al., 2004)
- (vi) Penetration-resistance drilling (Rinn et al., 1996; Mäkipää & Linkosalo, 2011; De Ridder et al., 2011; Rinn, 2012)
- (vii) Ultrasonic imaging (Bucur, 2003b)
- (viii) β-ray imaging (Phillips, 1960)
- (ix) γ-ray imaging (Laufenberg, 1986; Macedo et al., 2002)

In wood densitometry, X-rays have been successfully applied with the following methods:

- (i) X-ray densitometry which is based on the 2D image of the projection of a strip of defined thickness (typically 2 mm) (Polge, 1966, Schweingruber et al., 1978; Cleaveland, 1983, 1986; Decoux et al., 2004; Bouriaud et al., 2005; Rathgeber et al., 2006; Tomazello et al., 2008). While initially done on x-ray sensitive film and analysed with an analogue densitometer, which provided greyscale values, this method is now typically based on digital sensors.
- (ii) X-ray computed tomography which is based on the 3D reconstruction of the volume of a wood sample from many images) (Mull, 1984; Lindgren, 1991a, 1991b; Macedo et al., 2002; Espinoza et al., 2005; zu Castell et al., 2005; Freyburger et al., 2009; De Ridder et al., 2011).

In 2D X-ray densitometry, the greyscale - density calibration is achieved by a step wedge, which is typically made from a material with similar absorption characteristics as wood. In this projection-based method, each step of the wedge gives a grey value that depends on density and thickness. In contrast, in CT, a grey value does not depend on thickness. Thus, in CT densitometry, an imaging phantom is used (Cook & Kairiukstis, 1990). An imaging phantom is consisted from preferably homogenous reference materials with different density but similar absorption characteristics with the scanned sample. Each material provides a conventionally-determined density and an average grey value. Thus, a linear regression between the conventionally-determined density and the grey value enables the calculation of the CT density for any grey value of the reconstructed volume.

1.3. Motivation

Wood density is a fundamental property because it correlates with several mechanical, morphological, physiological, and ecological properties (Cown & Ball, 2001; Espinoza et al., 2005; Chave et al., 2006).

In the timber industry, wood density is considered the most significant single indicator of wood quality because it is correlated to numerous properties such as mechanical strength and stiffness, compression, decay resistance, workability and larger yields of pulp (Cown et al., 1991; Cown & Harris, 1991; Koubaa et al., 2002; Espinoza et al., 2005; Chave et al., 2006; Knapic et al., 2007; Freyburger et al., 2009; Wessels et al., 2015).

In the context of global change, wood density is used to estimate the woody biomass of a forest in order to access the carbon storage of a forest source or of forest products (Chave et al., 2006; Freyburger et al., 2009; Seifert & Seifert, 2014; Magalhães & Seifert, 2015a; 2015b; Phiri et al., 2015).

In engineered wood products such as wood fibre, particle, flake or veneer panels, the internal density variations determine their physical and mechanical properties like hardness, bending strength and stiffness, porosity, internal bond strength, holding strength of nails and screws (Laufenberg, 1986;)

In the discipline of dendrochronology, wood density is also of great importance, since it provides additional contrast to optical tree ring measurements and additional parameters that can be correlated with climatic influences such as the latewood density (Cleaveland, 1986; Schweingruber & Kienast, 1986; Schweingruber, 1988; Cook & Kairiukstis, 1990; Briffa et al., 2002). In the broader sense of the term, dendrochronology includes many subdisciplines e.g. dendroarchaeology, dendrochemistry, dendroclimatology, dendroecology, dendroentomology, dendrogeomorphology, dendroglaciology, dendrohydrology, dendropyrochronology and dendroseismology (Fritts, 1976). Thus, for example, in dendroclimatology, wood density is considered a key parameter for climate reconstruction because of its strong correlation with climate (Hughes et al., 1984; D'Arrigo et al., 1992; Briffa et al., 1995; Briffa et al., 1998 cited in Bouriaud, et al., 2005).

Furthermore, dendrochronology uses wood density profiles which are a series of consecutive density measurements from the innermost to the outermost tree ring. The density profiles can be used for ring-wise measurements (e.g. ring width, earlywood ring width, latewood ring width, latewood width percentage, average ring density, average earlywood density, average latewood density, ring density standard deviation) and for statistical modelling of density in relation to ring width, growth conditions etc. (Cleaveland, 1983; Koubaa et al., 2002; Nocetti et al., 2011).

1.4. Identification of gaps of knowledge

The greyscale - density calibration can be influenced negatively by factors such as porosity, atomic numbers, quantum noise, artefacts related to topography, changes in the reconstruction algorithm, changes in the X-ray tube and the detector and aging of the X-ray tube (Phillips & Lannutti, 1997; Stoel et al., 2008). Most of the research studies were based

on medical CT scanners, which are quite limited in the ways the scan can be manipulated in terms of spatial resolution, voltage and current and thus are known to deliver quite homogeneous density results (Mull, 1984; Lindgren, 1991a, 1991b; Espinoza et al., 2005; Hou et al., 2007; Freyburger et al., 2009; Nikolova et al., 2009). In contrast, modern industrial cone beam CT scanners are fully customizable. The advent of industrial CT scanners has brought novel ways to analyse wood in terms of spatial and density resolution. However, there is not a standardized methodology of wood microdensitometry with industrial CT scanners to date, which substantially inhibits the comparability of results obtained with such machines.

2. Materials and Methods

2.1. Overall objective

To address the mentioned shortcomings, the research objective of this thesis was the contribution to the development of a robust methodology for accurate microdensitometry of wood samples with an industrial cone beam CT scanner. Within that context the study aimed at developing the methodological foundation for microdensitometry of *Pinus radiata* in a larger research project, so it was a logic choice to demonstrate the feasibility of the method on selected samples of that tree species.

The main objective of this thesis was the development of an accurate and robust methodology for the greyscale - density calibration of reconstructed volumes of wood samples.

As an additional objective, the greyscale - density calibration was applied for the creation of tree ring CT density profiles to show the feasibility of the method in radial density profiling. Further analysis of the density profiles from a forest and wood science perspective was beyond the goal of this study.

2.2. Summary of the methodology

The methodology can be summarized as follows (Figure 2):

- (i) The first stage of the methodology was the fabrication of an imaging phantom from reference materials with similar chemical composition to the wood samples. Stem discs of *Pinus radiata* were regarded as the wood samples.
- (ii) The second stage was the CT scanning of the wood samples including the imaging phantom on each scan.
- (iii) The third stage was the development of calibration equations that linked greyscale and density for each reconstructed volume. This was achieved by performing a regression between the conventionally-determined density and the grey value of the phantom's reference materials. Then, the calibration was validated by calculating the error between the conventionally-determined density and the CT density of extra reference materials.

Stage 1: Imaging phantom fabrication	Fabrication of the imaging phantom from reference materials with similar chemical composition to the wood samples
Stage 2: CT scanning	CT scanning of the wood samples including the imaging phantom on each scan
Stage 3: Greyscale - density calibration	Conventional density measurement of phantom's reference materials Grey value measurement of phantom's reference materials Greyscale - density calibration equations Validation of the greyscale - density calibration equations

Figure 2 - A synopsis of the methodology

2.3. Imaging phantom and wood samples

A first step for the fabrication of the imaging phantom (reference body serving for the greyscale - density calibration) was the selection of materials with different densities. Thus, fourteen slices of wood from eleven different tree species (*Acacia erioloba*, *Celtis africana*, two samples of *Eucalyptus cladocalyx*, *Eucalyptus gomphocephala*, *Eucalyptus grandis* × *Eucalyptus camaldulensis*, *Ochroma pyramidale*, *Picea abies*, *Pinus pinea* - heartwood, *Pinus pinea* - sapwood, two samples of *Pinus radiata*, *Pinus sp.*, and *Pinus sylvestris*) and one slice of polyoxymethylene (acetal) were cut. All the slices had a uniform thickness of 1 cm. Three stacks were formed by sticking the slices to each other with a double-sided tape (Figure 3).

The cell wall of wood consists from cellulose ($C_6H_{10}O_5$), hemicellulose, lignin ($C_9H_{10}O_2$, $C_{10}H_{12}O_3$, $C_{11}H_{14}O_4$) and pectin ($C_6H_{10}O_7$) and their density is ranging around 1.5 gr/cm^3 (Kellogg & Wangaard, 1969; Gibson, 2012). Acetal ($(CH_2O)_n$) is a polymer made up from the same chemical elements (carbon, hydrogen and oxygen) and has a close density ($1.41\text{-}1.42 \text{ gr/cm}^3$) to the cell wall. Thus, it was hypothesized that it could be used optionally as an extra reference material.

One of the objectives of this study was to show the feasibility of the greyscale - density calibration for reconstructed volumes of wood samples. Thus, fifty stacks of *Pinus radiata* stem discs from an earlier study (Fischer, 2011), which were cut from an equal number of trees, were selected as the wood samples (Figure 4). The trees were at half rotation age, between nine and eighteen years old. Furthermore, five discs were cut from each tree. The first disc was cut at base height (0.1 m), the second disc was cut at breast height (1.3 m) and the third disc was cut at the beginning of the canopy. The fourth and the fifth disc were cut at one third and two thirds of the canopy's length respectively.

The minimum, maximum and average diameter was calculated for the discs of each height, without including the bark (Table 1).

The stems disks and some of imaging phantom materials were air-dried for at least a year. Their moisture content was measured on samples before scanning. However, there was a flooding incident at the workshop, which added moisture to the stem disks.

The stems disks were air-dried for at least a year and their moisture content was measured on samples and found to be 12%. The imaging phantom materials were oven-dried at 60°C and left to reach the same moisture equilibrium.



Figure 3 - The imaging phantom



Figure 4 - A part of the Pinus radiata stacks which were used for testing the method

Table 1 - The minimum, maximum and average diameter of the discs of each height

Discs from	Diameter (cm)		
	Minimum	Maximum	Average
Height 1 (0.1m)	14.6	28.7	22.4
Height 2 (1.3m)	12.7	27.9	20.0
Height 3 (Beginning of canopy)	11.3	26.5	17.8
Height 4 (Beginning of canopy + 1/3 of canopy's length)	6.9	20.3	13.2
Height 5 (Beginning of canopy + 2/3 of canopy's length)	3.4	13.3	7.7

2.4. CT scanning procedure

The *P. radiata* stacks were scanned in a General Electric Phoenix VTomeX L240 CT scanner with the following scheme:

- (i) Each *P. radiata* stack was scanned separately and the three phantom stacks were included in every scan. The position of the phantom stacks was wherever there was available space and thus was variable. All the objects were placed onto packaging foam which was placed onto the rotating metallic chuck of the CT scanner in order to prevent artefacts from metal and X-ray interaction. All the objects were stuck together by poster putty in order to prevent movement during their rotation. Furthermore, all stacks were scanned in four continuous days with equal hot and dry climate. Additionally, the air conditioner was used in the CT scanner room to prevent moisture and temperature fluctuations.
- (ii) The spatial resolution (volume represented by a voxel) was increased to the point that the largest *P. radiata* stack could exactly fit in the acquired X-ray images. The resulting position of the X-ray detector and the rotating chuck were kept constant for all the scans to avoid any fluctuations to the measured grey value of the X-ray images.
- (iii) Before placing any objects inside the scanner and starting a new scan, the X-ray detector was auto-calibrated to the signal of the X-rays. This digital procedure ensures that the detector receives an even X-ray signal. After the auto-calibration, the CT scanner was left to stabilize for 10 minutes.
- (iv) Upfront, the voltage and the amperage were adjusted empirically by experimentation to deliver the best images. Specifically, a stem disc stack was scanned with various combinations of voltage and amperage. The combination of 200 kV and 200 μ A was

selected because it provided the ideal brightness and contrast on the reconstruction of the disc stack. All further disc stacks were scanned with these parameters.

(v) Furthermore, a copper (Cu) (1mm) filter and an aluminium (Al) (1mm) filter were tested, but none was used for the scans because they affected the contrast.

(vi) The following parameters were set as shown on Table 2:

Table 2 - The settings of the scans

Parameter	Value
Voltage	200 kV
Amperage	200 μ A
Image resolution	2048 \times 2048
Perimetrical images	3000
Image binning	No
Images acquired/skipped	1 acquired/1skipped
Image exposure time	333ms
Scan duration	36'
Region of Interest (ROI)	Yes

After the scans, the 'General Electric Phoenix DatasX' software created the reconstructed volumes of the scanned objects. Beam hardening correction was included in the reconstruction to avoid beam hardening effects which are substantial if objects of different size and density are scanned. The effect is based on the fact that the X-ray tube does not emit a monochromatic radiation beam but it emits a beam of X-rays with a wider distribution of frequencies and with different penetration ability. Harder X-rays will penetrate longer distances while softer X-rays will penetrate less easily. This phenomenon leads to a hardening of the beam with increasing distance through the object. This means that the beam penetration is higher at the end of the penetration through the object. Thus, an internal procedure during the reconstruction process is applied to compensate for such effects.

Examples of image acquisition from a CT scan and of a reconstructed volume can be seen on Figure 5, 6, and 7.

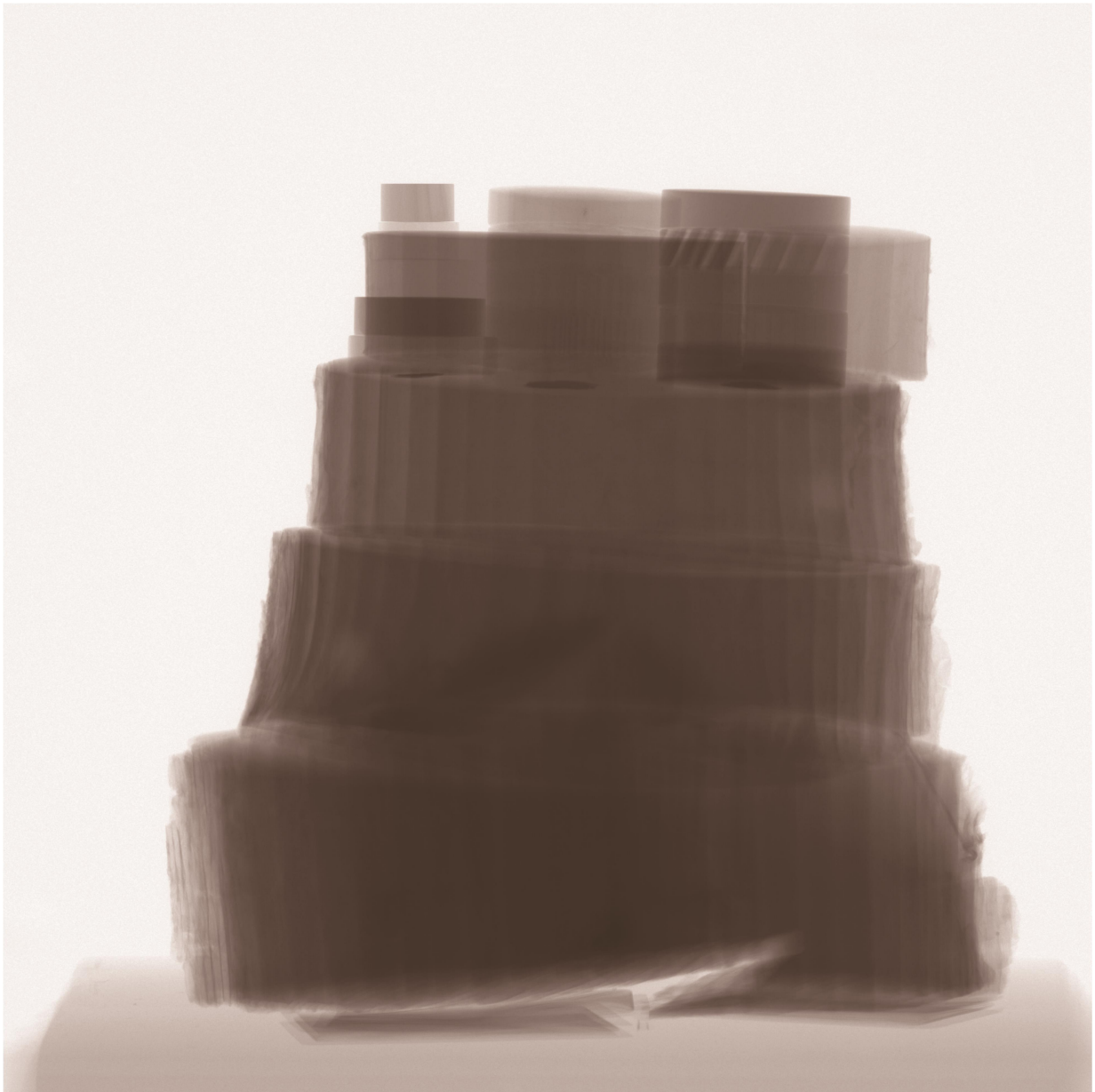


Figure 5 - An X-ray image from a CT scan

*This image is one of the 3000 perimetrical X-ray images of a scan from which a volume was reconstructed. It includes the five *P. radiata* stem discs and the imaging phantom.*

Darker pixels denote reduced X-ray penetration and thus increased linear attenuation coefficient.

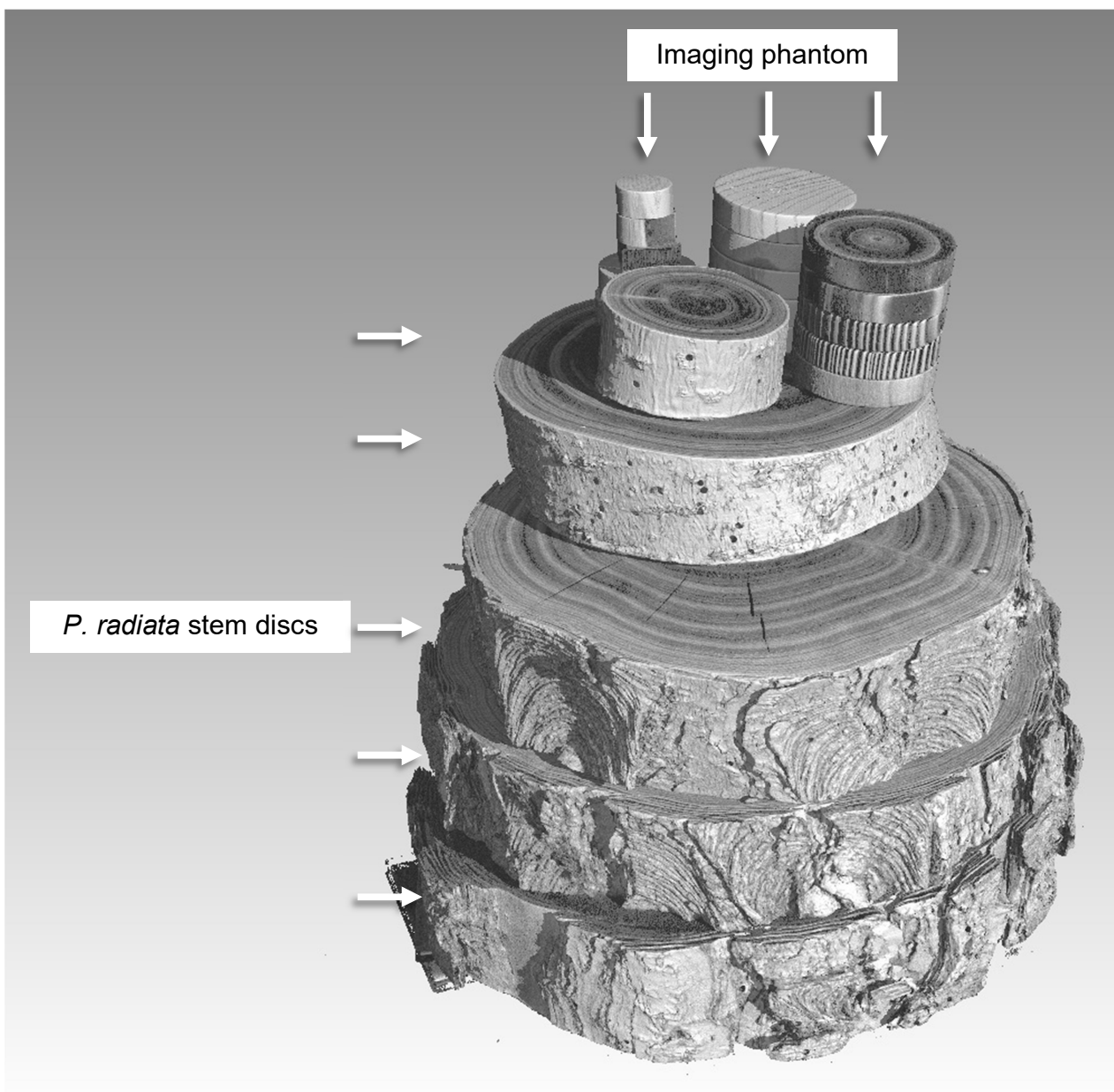


Figure 6 - A reconstructed volume

The reconstructed volume includes five stem discs from a *P. radiata* tree and the imaging phantom.

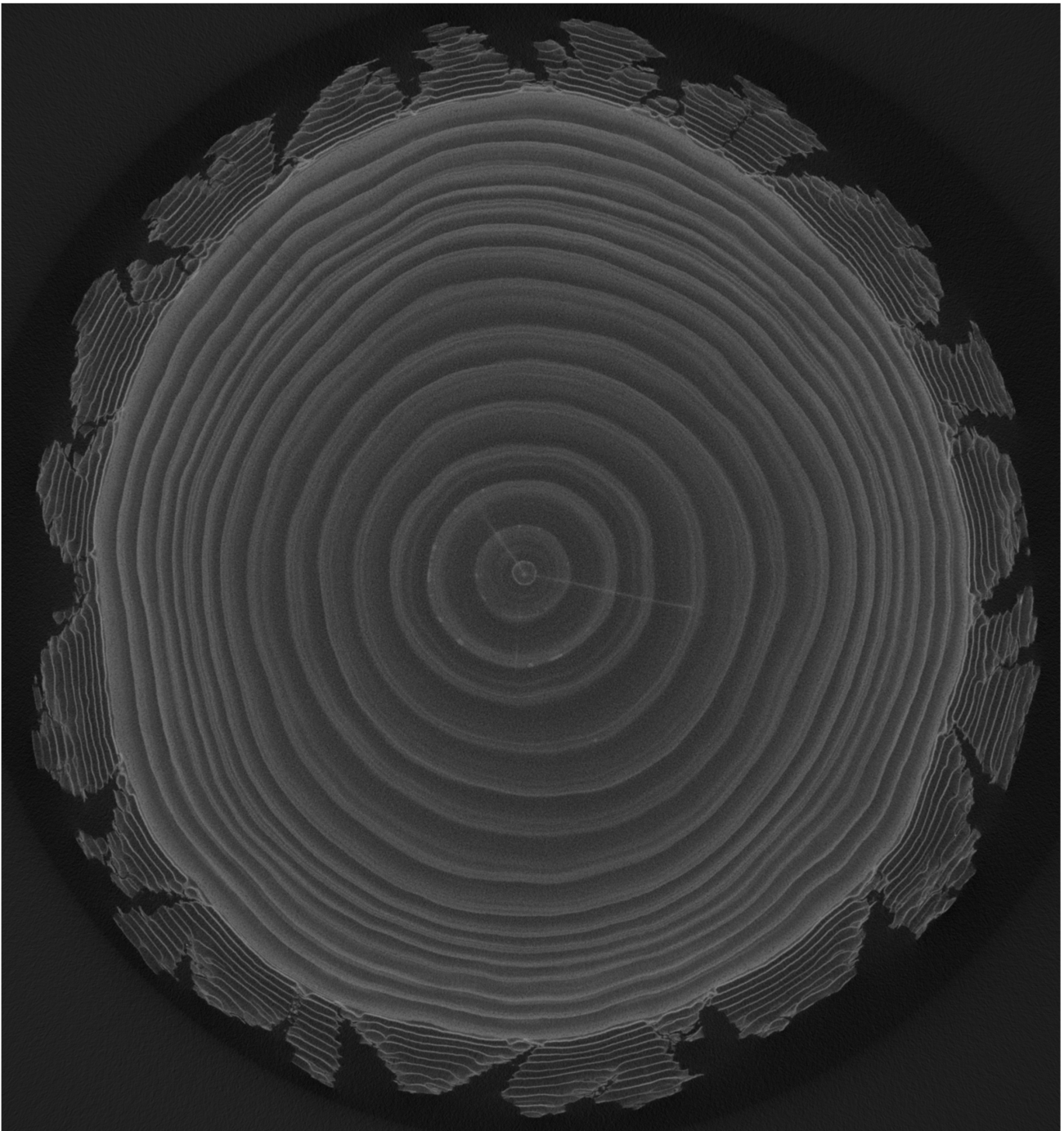


Figure 7 - A cross-section of a reconstructed volume

Brighter pixels represent higher densities and darker pixels, lower densities.

2.5. Greyscale - density calibration

Conventional density measurement of the phantom slices

In order to determine the density of the slices conventionally, their volume was measured with a digital calliper and their weight with a digital scale.

Grey value measurement of the phantom slices

A batch of cross-sectional 'tiff' images with spacing of 1mm was exported from every reconstructed volume with the help of 'VGStudio MAX' and then it was imported into the 'ImageJ' software (*File* → *Import* → *Image Sequence*) (Figure 8). On 'ImageJ', the cross-sectional images were also calibrated for distance measurements (*Image* → *Properties*) by using the spatial resolution provided by 'VGStudio MAX', e.g. 0.14939 mm/voxel. This was necessary because the spatial resolution information was not imported into the images and had to be added manually. Additionally, the images were coloured with pseudocolour in order to make it easier to distinguish between earlywood and latewood (*Image* → *Lookup Tables* → *Fire*). Moreover, this did not affect the measurements. Finally every batch of images was saved as one 'tiff' file in order to speed up the measurement process.

The average grey value of a slice was measured by locating an image where that slice was present. Then the area of the slice was selected by applying a threshold tool (*Toolset* → *Wand tool*) and after that by measuring the average grey value of the pixels of the selected area (*Analyze* → *Measure*). The average grey value was taken from only one image in order to speed up the measurement process.

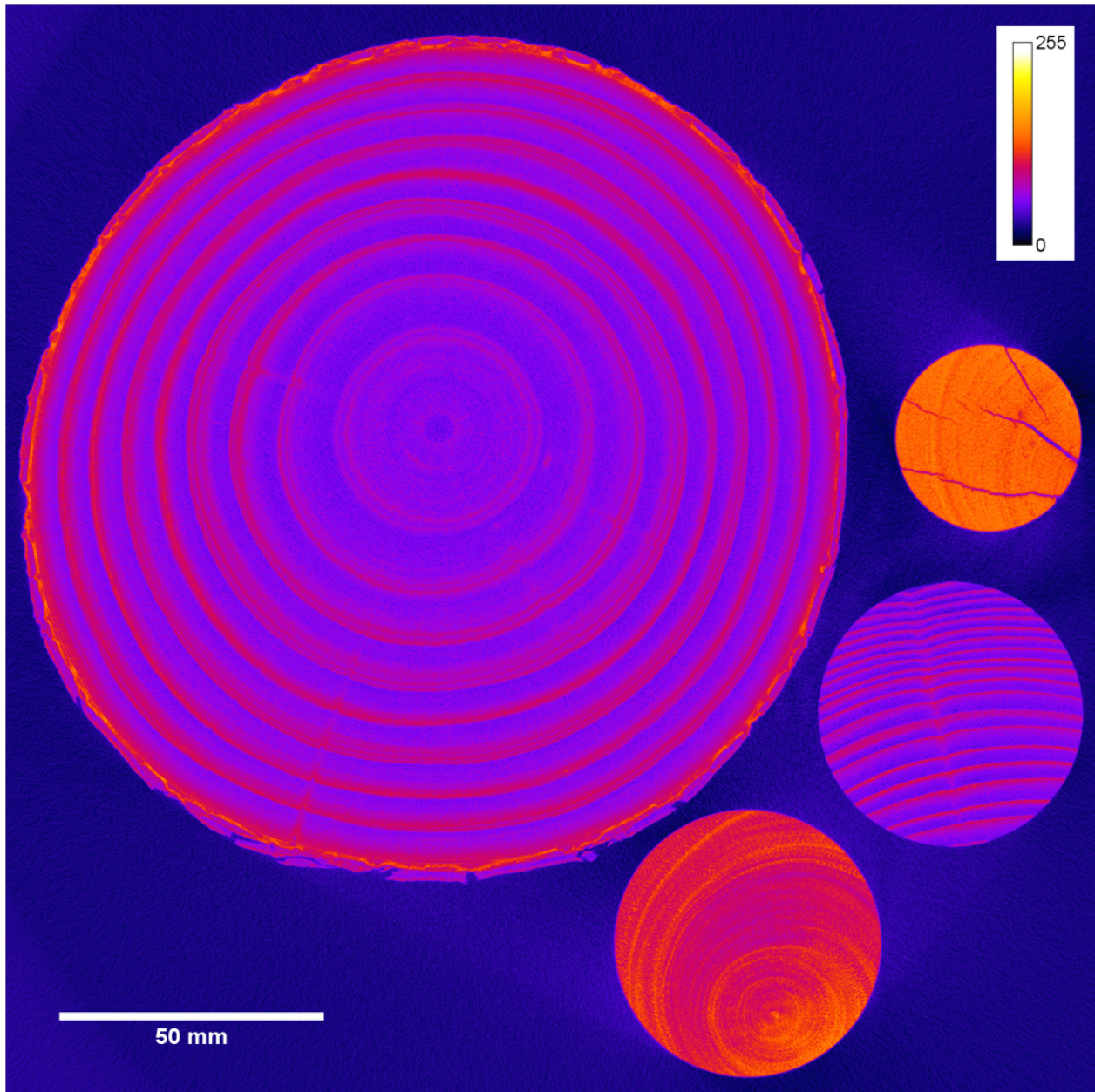


Figure 8 - A cross-sectional image with pseudocolour

A P. radiata stem disk and three phantom slices are visible.

The values of the pixels increase from 0 to 255 in response to density.

Greyscale - density calibration equations

A traditional least squares regression minimizes the squares only in the direction of the y-axis. This is correct if measurement errors are present only on the y-axis direction. If there are measurement errors also on the x-axis variable then the traditional least squares regression produces biased results. In our case we can assume that the grey values are also measured with a certain error. Thus the linear reduced major axis (RMA) regression was chosen, which adjusts the fitted line accordingly to prevent a bias (Warton et al. 2006; Seifert et al., 2010). With the help of the programming language R, a RMA regression was performed for each reconstructed volume between the conventionally-determined density of the slices and the grey value of the slices, in order to obtain a calibration equation (Appendix A). A calibration equation is a volume-specific linear equation, which translates a given grey value to a certain CT density (Equation 3).

$$\rho_{CT} = slope \cdot gv + intercept$$

Equation 3 - Translation of a grey value into CT density

ρ_{CT} : CT density

gv : Grey value

Validation of the greyscale - density calibration equations

The CT density and the CT density error (absolute and percent) of the three validation slices were calculated for each reconstructed volume (Equation 4 and 5). Then, the mean absolute error and the mean percent error of the three validation slices were calculated for each volume and plotted in two histograms.

$$\varepsilon = |\rho_C - \rho_{CT}|$$

Equation 4 - The absolute error of the CT density of a phantom slice

ε : Absolute error

ρ_C : Conventionally-determined density

ρ_{CT} : CT density

$$\eta = \left| \frac{\rho_C - \rho_{CT}}{\rho_C} \right| * 100$$

Equation 5 - The percent error of the CT density of a phantom slice

η : Percent error

ρ_C : Conventionally-determined density

ρ_{CT} : CT density

2.6. Tree ring CT density profile

The CT density measurement was demonstrated by constructing the tree ring CT density profile of five stem discs from the same tree.

For each cross-sectional image, a rectangular strip starting from the end of the pith and ending at the end of the outermost ring was drawn (Figure 9). The width of the strip was specified to be 25 pixels by using the 'Specify' function (*Edit* → *Selection* → *Specify*). Then, the 'Plot Profile' tool (*Analyze* → *Plot Profile*) was used to create a table of the average grey value along the strip.

Then, the table was copied on 'MS Excel' (*Plot Profile* → *Copy*) where the CT density was calculated for each grey value by applying the volume-specific calibration equation (Table 3). Lastly, the table of the CT density profile was plotted. The mean CT density of each profile was also calculated.

As an optional step, the strips were copied (*Edit* → *Copy to System*), they were pasted on their corresponding graph and then they were scaled to the same length of the graph. This way of displaying density profiles shows the density differences in the radial direction and their correspondence to the different years.

A strip width of one pixel (0.149 mm) would produce a CT density profile influenced strongly by local density fluctuations since due to the high geometrical resolution the grey values of small anatomical features such as resin ducts or even cell lumina and walls will be picked up. In this case, a low pass filter could be applied to smooth the profile. However, a typical kernel filtering, as applied in signal processing, would work in radial direction which represents cell formation over time in a tree stem. A filter with a symmetric smoothing kernel would mix cells that were formed before and after the point of interest and thus include future density values which would be not logical. An asymmetric kernel would still include density values of cells that were formed before the point of interest. Thus, it is better to average in a tangential direction. Consequentially, a strip width between 10 (1.49 mm) and 25 (3.73 mm) pixels could provide a reasonable average density, acting essentially like a low pass filter (Figure 10, 11, and 12). Furthermore, it was found that in experiments with strips larger than 25 pixels in width would not produce accurate average density values, because of the curvature of the tree rings would again mix cells that were formed at different times.

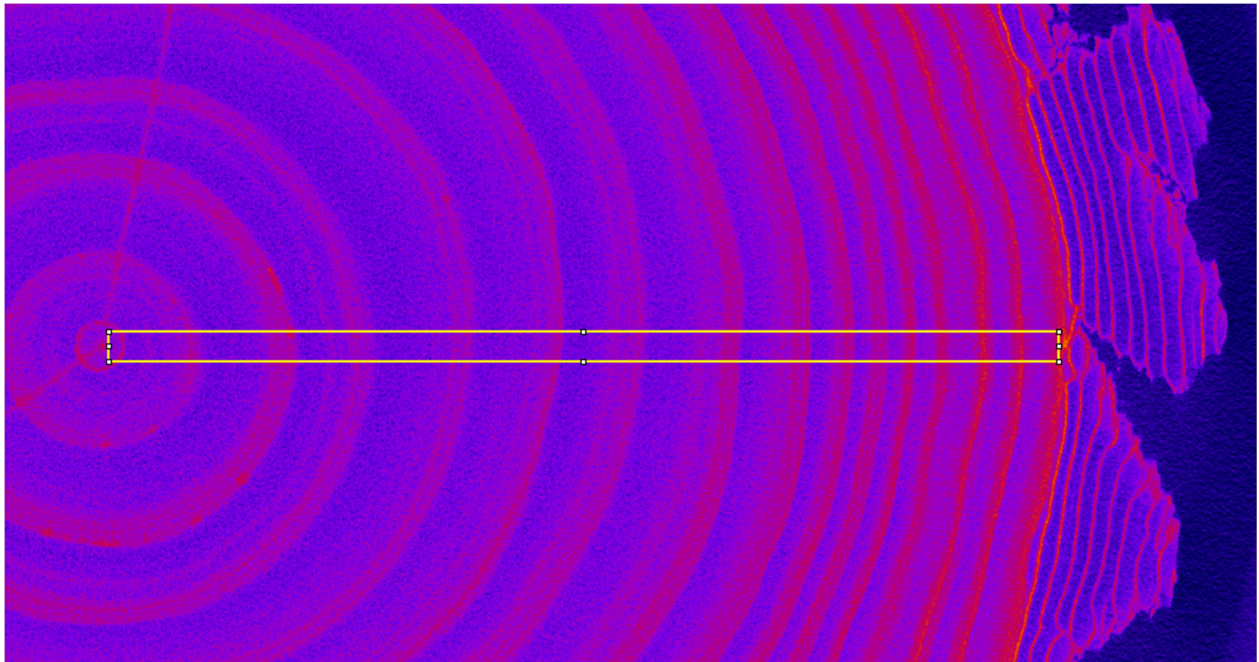


Figure 9 - CT density profile selection on Image J

Each column of pixels inside the selection has a width of 25 pixels. The 'Plot Profile' tool took the average grey value from every column and its distance starting from the left.

Table 3 - Example of a CT density profile table

A part of the CT density profile table of stem disc 1. The CT density results from the application of the volume-specific calibration equation.

Distance from pith (mm)	Grey value	CT density (g/m ³)
0.00	64.00	0.435
0.15	61.72	0.408
0.30	62.68	0.419
0.45	63.08	0.424
...

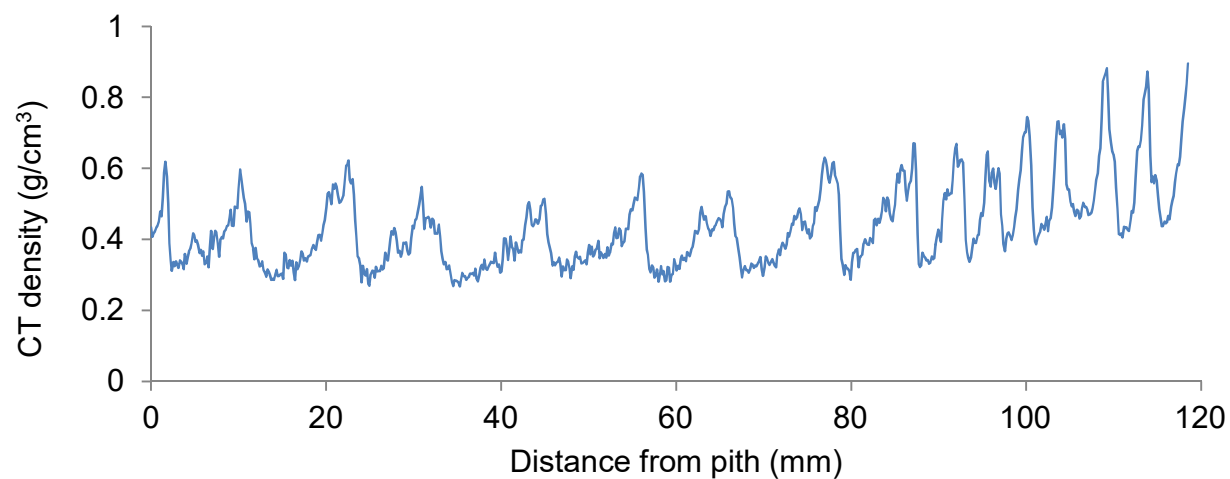
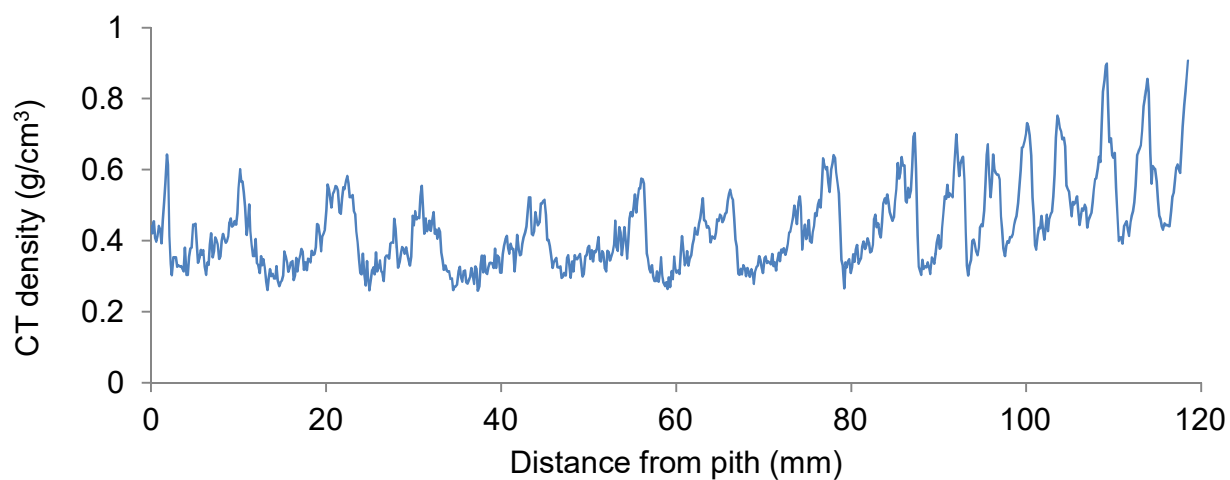
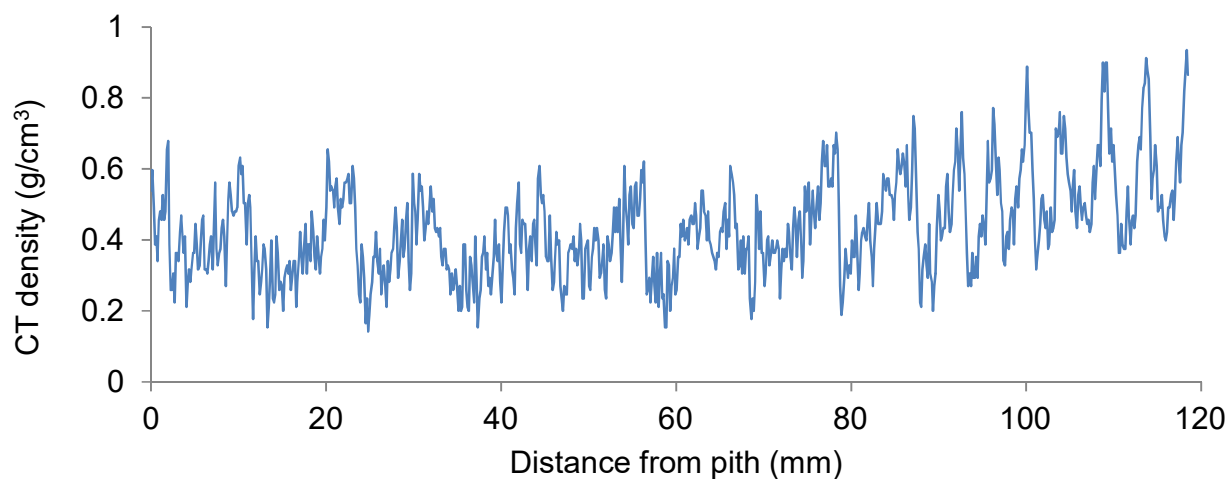


Figure 10, 11 and 12 - The effect of the strip width (1, 10, and 25 pixels) on the density profile

2.7. Potential sources of CT density error

2.7.1. Homogeneity of phantom slices

Due to local density fluctuations or system noise, a large deviation in the grey value of the cross-sectional images (spacing of 1 mm) of a phantom slice could affect the regression and therefore the calibration equation. Thus, a large deviation in the grey value could be a potential source of CT density error. For this reason, the standard deviation of all the cross-sectional images of each phantom slice from five reconstructed volumes was calculated (15 slices \times 5 reconstructed volumes = 75 slices).

2.7.2. Number of phantom slices

Another potential source of CT density error could be the number of phantom slices used for the regression. An inadequate number of phantom slices would affect the reliability of the measured CT density. In order to determine the optimal number of phantom slices, regressions with 4, 6, 8, 10, and 12 phantom slices were performed for five reconstructed volumes (5 regressions with different number of slices \times 5 reconstructed volumes = 25 regressions).

3. Results

3.1. Greyscale - density calibration

Conventional density measurement of the phantom slices

The conventionally-determined density of the wood slices was ranging from 0.21 g/cm³ to 1.25 g/cm³ and the conventionally-determined density of acetal was 1.43 kg/m³ (Table 4).

Table 4 - Air-dry conventionally-determined density of the phantom slices

Scientific name	Common name	Density (g/cm ³)
<i>Ochroma pyramidale</i>	Balsa	0.21
<i>Pinus sp.</i>	Pine	0.36
<i>Pinus radiata</i> - sample b	Radiata Pine	0.39
<i>Pinus radiata</i> - sample a	Radiata Pine	0.41
<i>Picea abies</i>	Norway Spruce	0.44
<i>Pinus sylvestris</i>	Scots Pine	0.55
<i>Celtis africana</i>	White Stinkwood	0.60
<i>Eucalyptus grandis</i> × <i>Eucalyptus camaldulensis</i>	Rose Gum and River Red Gum hybrid	0.73
<i>Pinus pinea</i> - sapwood	Stone Pine	0.76
<i>Eucalyptus cladocalyx</i> - sample b	Sugar Gum	0.80
<i>Pinus pinea</i> - heartwood	Stone Pine	0.82
<i>Eucalyptus gomphocephala</i>	Tuart	0.90
<i>Eucalyptus cladocalyx</i> - sample a	Sugar Gum	0.97
<i>Acacia erioloba</i>	Camel Thorn	1.25
<i>Polyoxymethylene</i>	Acetal	1.43

Grey value measurement of the phantom slices

Six phantom slices (*Acacia erioloba*, *Eucalyptus gomphocephala*, *Ochroma pyramidale*, *Pinus pinea* - heartwood, *Pinus sylvestris*, and *Polyoxymethylene*) were selected for the greyscale - density calibration and three (*Eucalyptus cladocalyx* - sample a, *Picea abies*, and *Pinus radiata* - sample a) were selected for the validation of the calibration. Ideally, more slices would offer greater reliability to the greyscale - density calibration (see 3.3.2 Number of phantom slices).

Greyscale - density calibration equations

The fifty regressions had a mean coefficient of determination $R^2=0.998$ and p-values <0.001 (Appendix B) (Figure 13). An $R^2>0.99$ was observed for 100% of the regressions and an $R^2>0.995$ for 96% of the regressions. Thus, it can be concluded that there is a strong correlation between conventionally-determined density and grey value.

Acetal lined up visually with the wood slices and increased the coefficient of determination in the regressions. Thus, it was concluded that acetal's different chemical composition was similar enough to wood and had not a significant effect on its grey value.

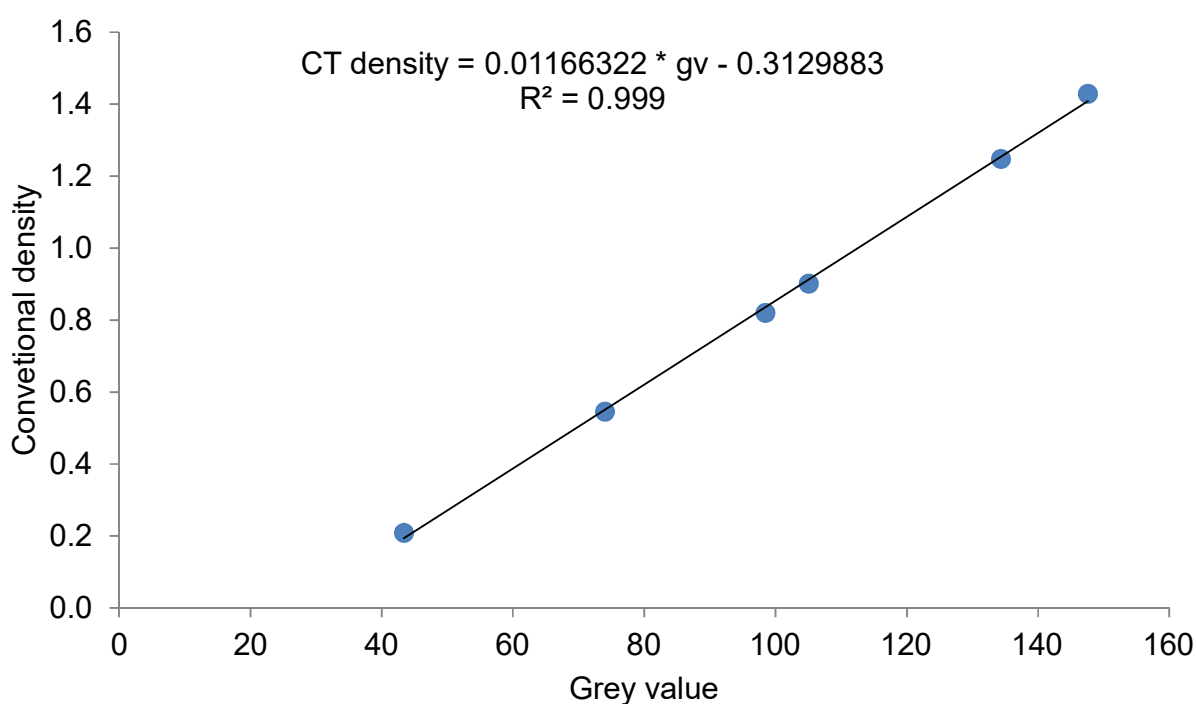


Figure 13 - One of the fifty greyscale - density regressions

As a test, the calibration equations were solved for the same grey value range (40-90) and gave CT densities with a large dispersion (Figure 14). Thus, it was concluded that the calibration equations varied significantly. As a consequence, a sole calibration equation could not be derived.

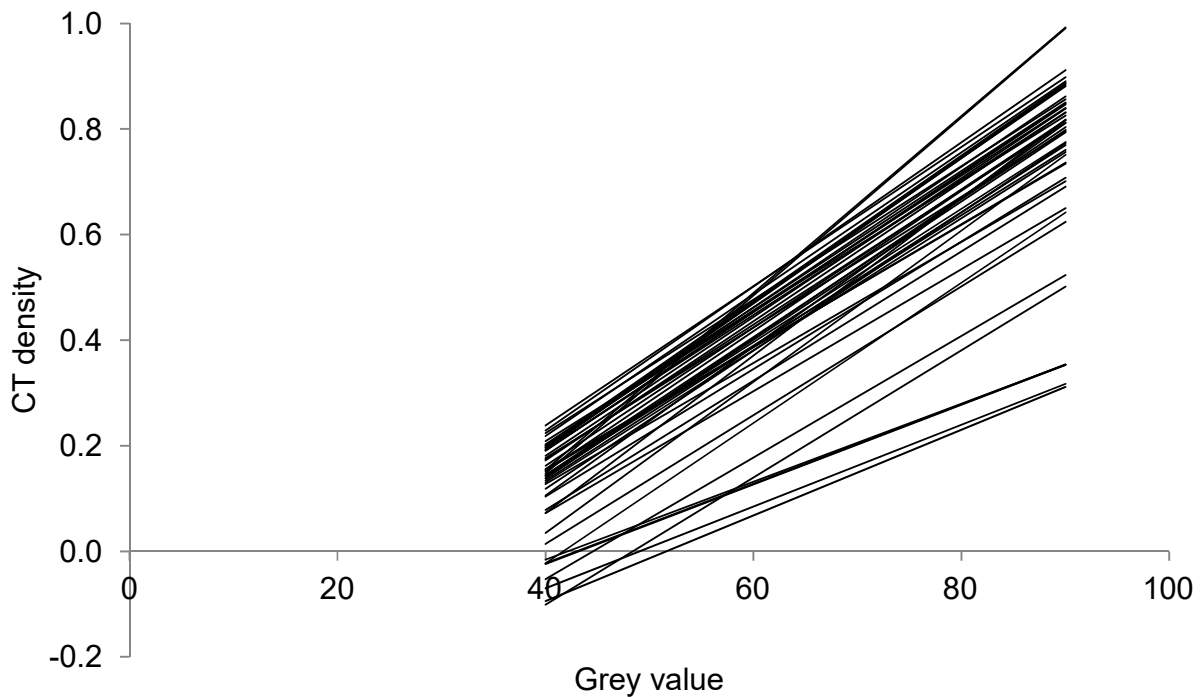


Figure 14 - The dispersion of the calibration equations

The equations were solved for the same grey value range.

Validation of the greyscale - density calibration equations

The absolute CT density error of the reconstructed volumes was ranging from 0.002 - 0.026 g/cm³ and had a mean of 0.008 g/cm³ ($\sigma=0.004$). Specifically, the absolute CT density error was smaller than 0.01 g/cm³ for 74% (n=37) of the reconstructed volumes, it was ranging between 0.01 and 0.02 g/cm³ for 24% (n=12) of the volumes and it was ranging from 0.02 to 0.03 g/cm³ for 2% (n=1) of the volumes (Figure 15).

The percent CT density error of the reconstructed volumes was ranging from 0.4% - 4.4% and had a mean of 1.4% ($\sigma=0.7$). Specifically, the percent CT density error was smaller than 1% for 30% (n=15) of the volumes, it was ranging between 1 and 2% for 52% (n=26) of the volumes, it was ranging between 2 and 3% for 16% (n=8) of the volumes and it was larger than 3% for 2% (n=1) of the volumes (Figure 16).

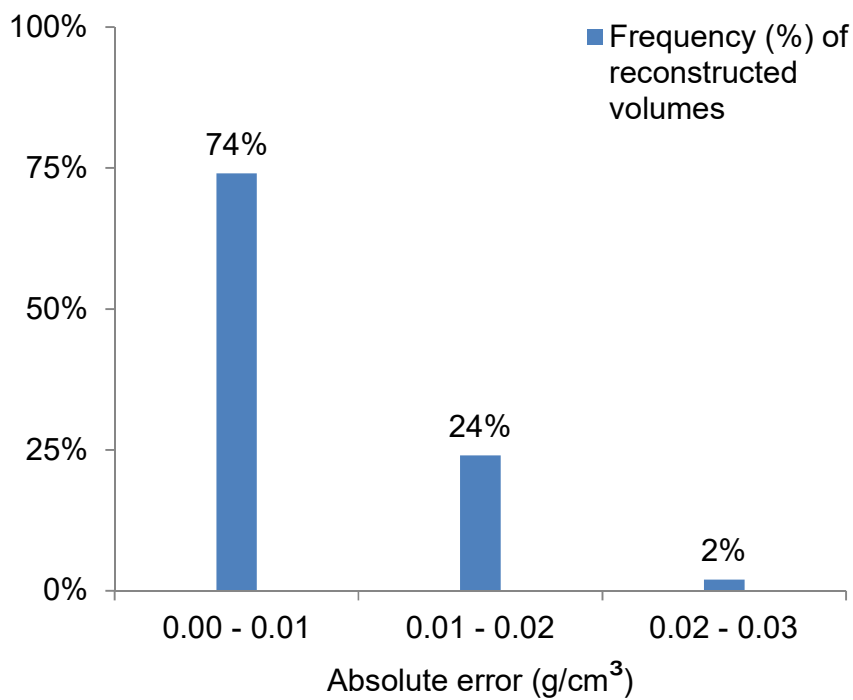


Figure 15 - The frequency of reconstructed volumes per CT density error

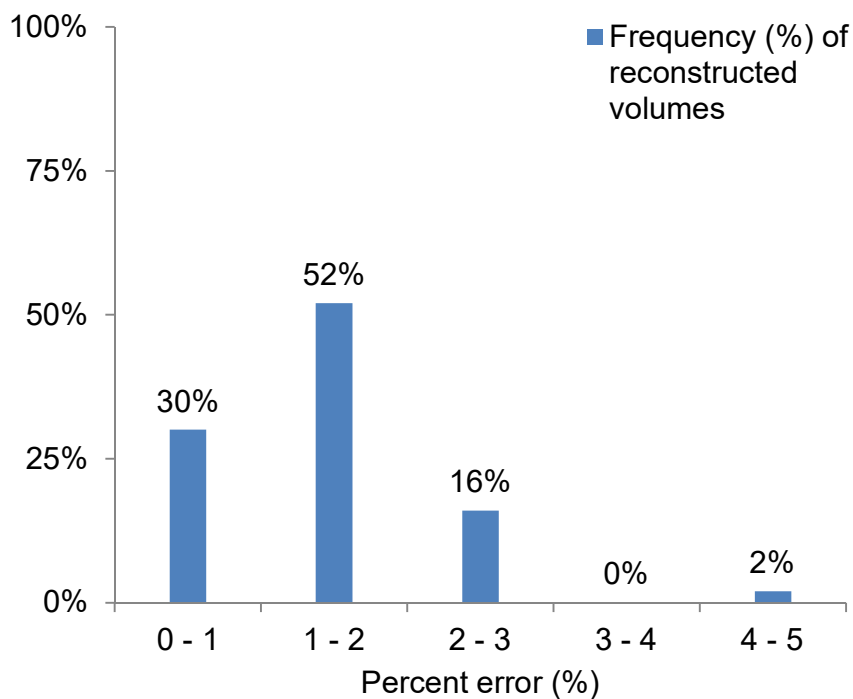


Figure 16 - The frequency of reconstructed volumes per CT density error (%)

3.2. Tree ring CT density profile

The density profiles showed the expected earlywood - latewood pattern with the characteristic upward trend (Figure 17, 18, 19, 20, and 21). The density had a reasonable spread between earlywood and latewood. The average density of each stem disc was also reasonable (Table 5). However, the outmost rings had a distinct increased density.

Table 5 - The mean CT density of each stem disc

Profile number	Average CT density g/cm^3
1	0.44
2	0.43
3	0.41
4	0.45
5	0.46

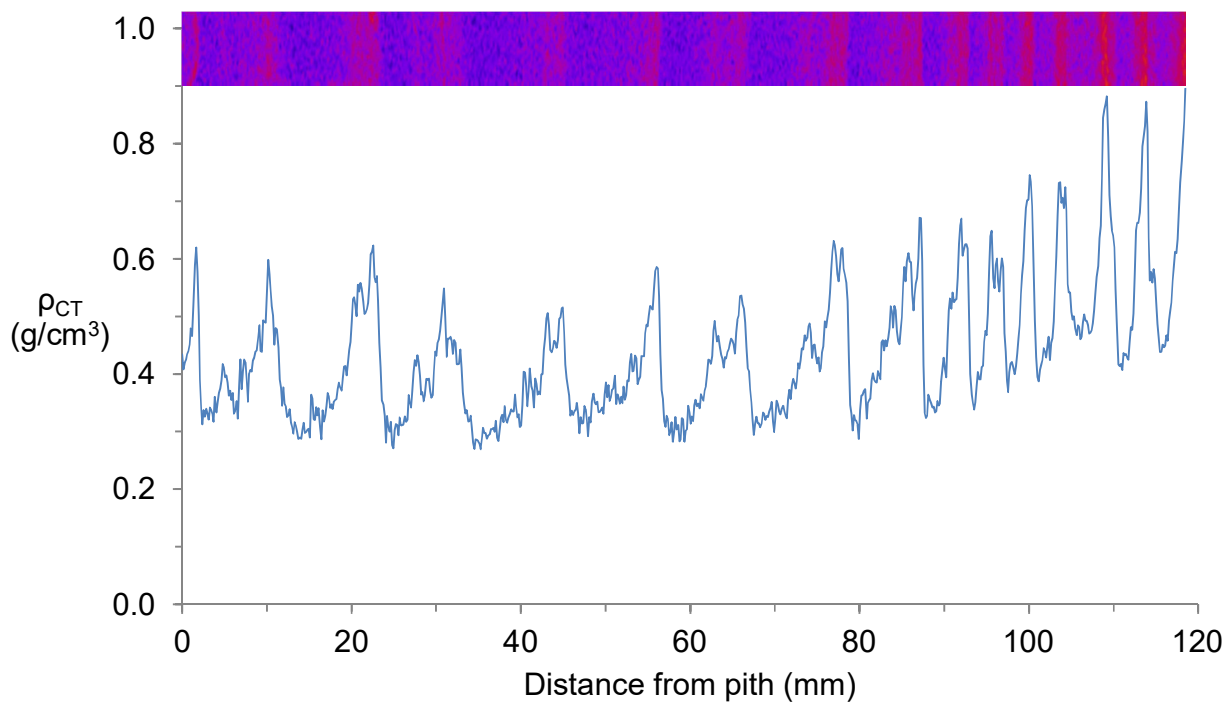


Figure 17 - The CT density profile of stem disc 1

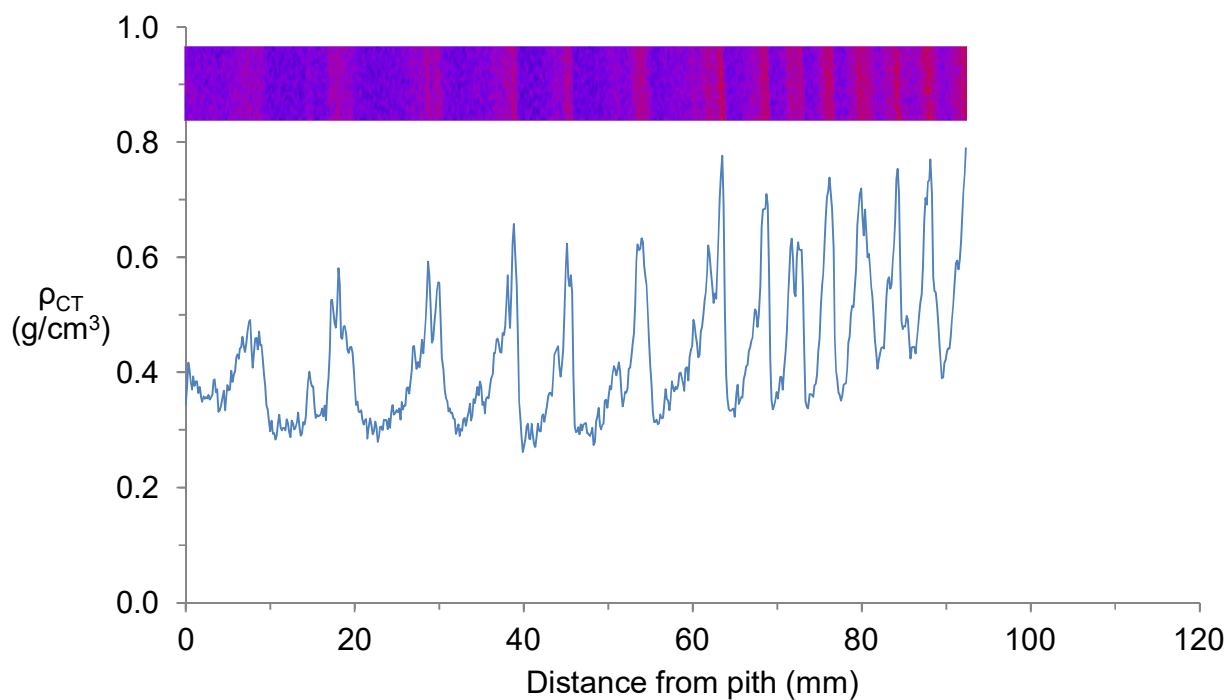


Figure 18 - The CT density profile of stem disc 2

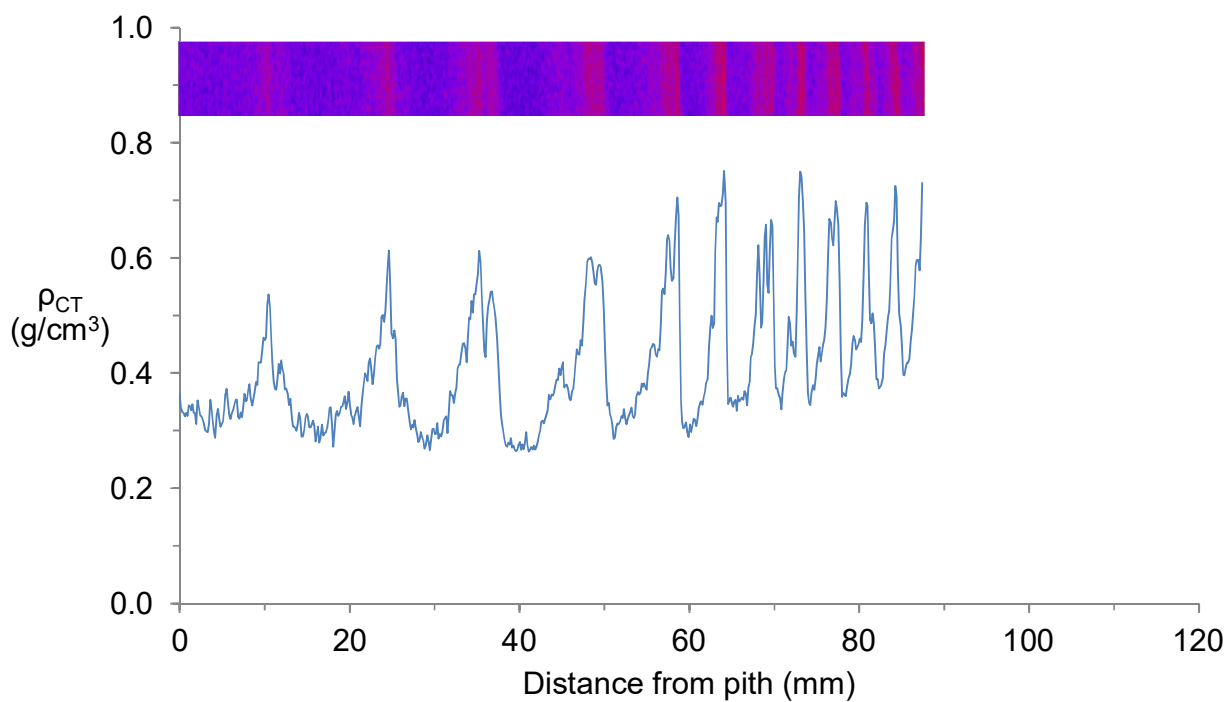


Figure 19 - The CT density profile of stem disc 3

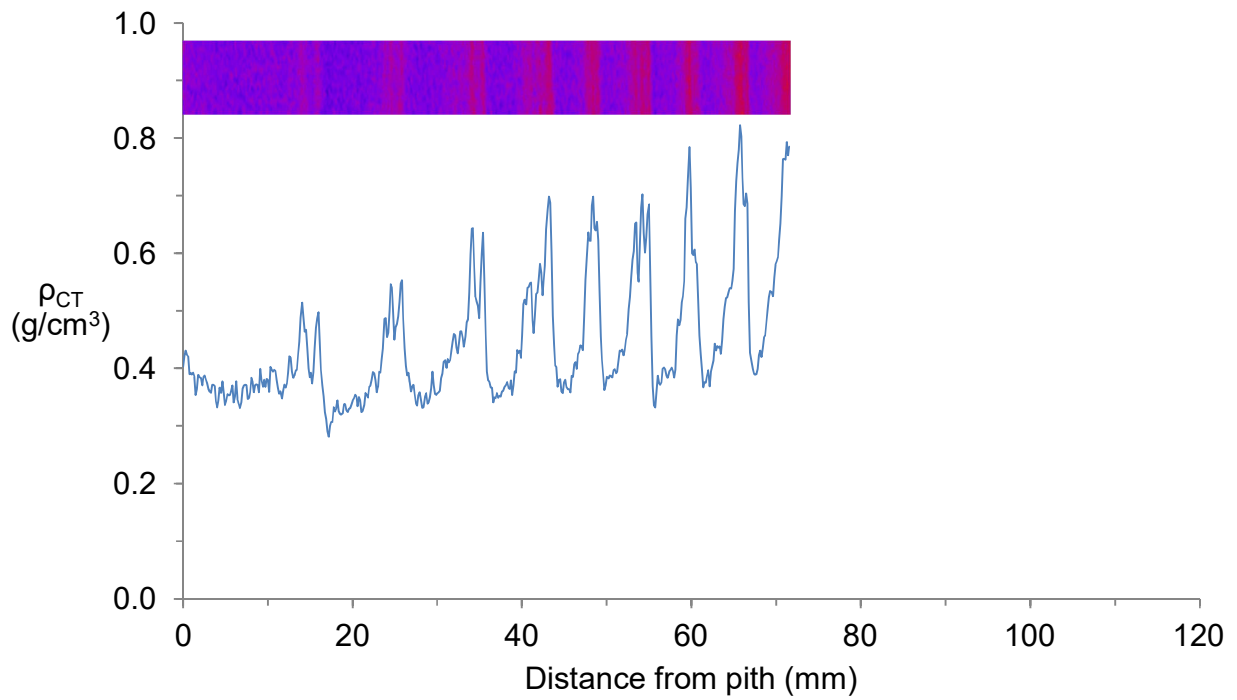


Figure 20 - The CT density profile of stem disc 4

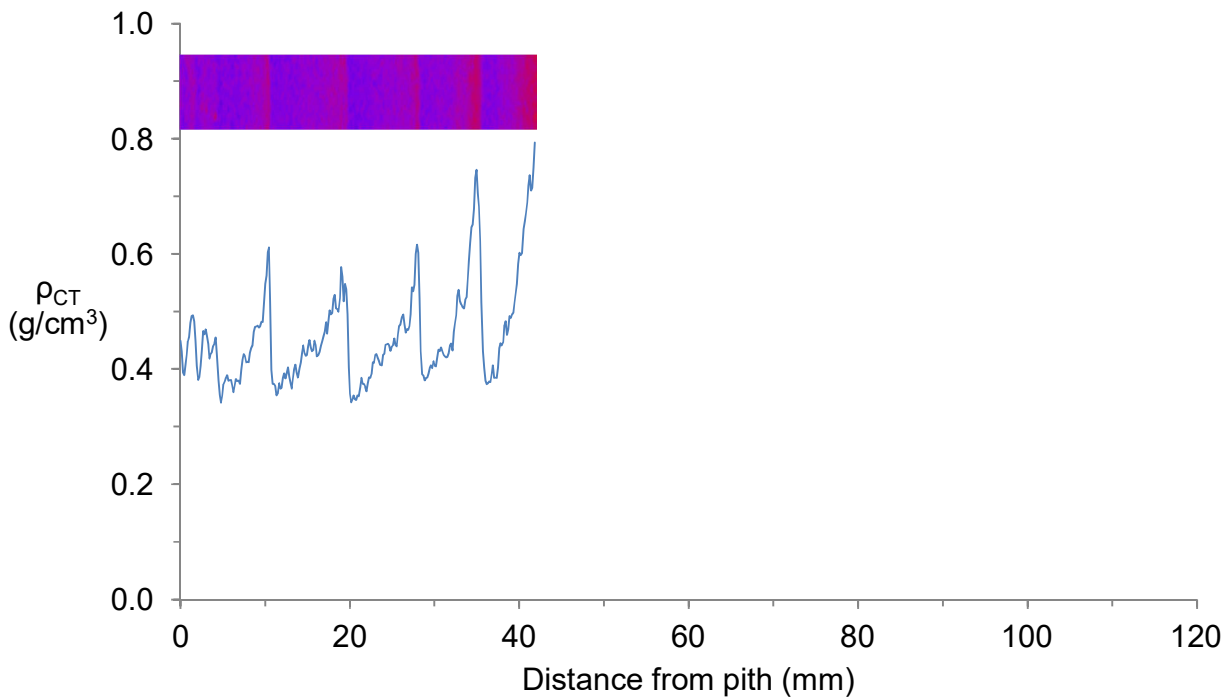


Figure 21 - The CT density profile of stem disc 5

3.3. Potential sources of CT density error

3.3.1. Homogeneity of phantom slices

The standard deviation in the grey value of the cross-sectional images was $s < 1$ for 95% of the phantom slices (71 out of 75 slices). The 100% of the slices had a standard deviation $s < 1.5$. Therefore, the deviation in the grey value of the cross-sectional images of a phantom slice has a small or negligible effect on the conventional density - grey value regression.

3.3.2. Number of phantom slices

In the following graph (Figure 22), each pair of confidence intervals (95%) is the average of five regressions from an equal number of reconstructed volumes. The colour denotes the number of phantom slices used.

It can be observed that the more the materials, the narrower the confidence intervals. Thus, it can be concluded that the reliability of a CT density calibration equation increases with the number of phantom slices used in the regression. In this study, a 10 material regression is the optimal, since a 12 material regression does not offer narrower confidence intervals.

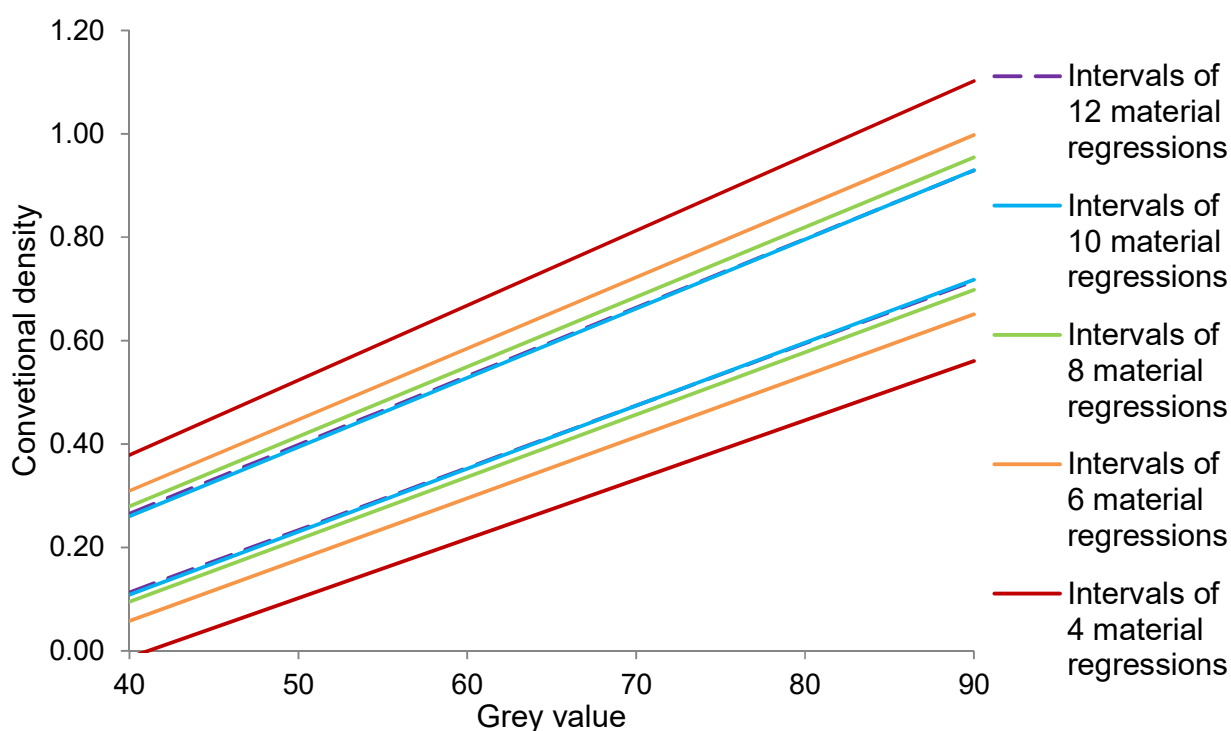


Figure 22 - The confidence intervals of regressions with 4, 6, 8, 10, and 12 materials

4. Discussion

4.1. Accuracy and repeatability of the greyscale - density calibration

4.1.1. CT density error

It can be concluded that the greyscale - density calibration was achieved with a small amount of error and a high repeatability because:

- (i) The absolute CT density error of the reconstructed volumes was ranging from 0.002 - 0.026 g/cm³ with a mean of 0.008 g/cm³ ($\sigma=0.004$).
- (ii) The percent CT density error of the reconstructed volumes was ranging from 0.4% - 4.4% with a mean of 1.4% ($\sigma=0.7$).
- (iii) For 98% of the reconstructed volumes, the absolute CT density error was smaller than 0.02 g/cm³ and the percent CT density error was smaller than 3% (Figure 15 and 16).

Likewise, it can be concluded that the creation of the tree ring CT density profiles (Figure 17, 18, 19, 20 and 21) was also achieved because:

- (i) The reconstructed volume that was used for the tree ring CT density profiles had an absolute CT density error of 0.003 g/cm³ which indicates a small amount of error in other CT density values.
- (ii) The observed air-dry CT density is consistent with the reported air-dry density of *P. radiata*. The mean CT density of the profiles was ranging from 0.41 to 0.46 g/cm³ while the reported density of *P. radiata* was about 0.48 g/cm³ in 10 to 20 year old trees (Forest Products Commission Western Australia, 2015).

However, the density of the outmost rings was rather high, which can be attributed to beam hardening or to an increased content of resin in that sapwood region.

4.1.2. Homogeneity of phantom slices

The grey value of the cross-sectional images did not deviate significantly ($s<1$) for 95% of the measured phantom slices (71 out of 75 slices). Thus, any inhomogeneity, due to the earlywood and latewood pattern or due to system noise, had a small or negligible effect on the deviation of the grey value and therefore to the greyscale - density calibration.

4.1.3. Number of phantom slices

Six phantom slices were used for the greyscale - density calibration and three for the validation of the calibration. It was observed that a higher number of phantom slices increase the reliability of the calibration equations. Therefore, greyscale - density calibrations with more phantom slices could have possibly reduced the CT density error.

4.1.4. Chemical composition of phantom slices

The measured grey value of a phantom slice is defined among others by its chemical composition. For this reason, the chemical composition of the materials of a phantom should be similar to the objects of interest (Phillips & Lannutti, 1997; Stoel et al., 2008). The difference in density between species is not an effect of different chemical composition but it depends on the proportion of the cell wall material and air in dry wood. Thus, air-dry wood density can range from very light wood such as *Ochroma pyramidale* (150 kg/m^3) to very dense wood such as *Guaiacum officinale* (1300 kg/m^3). The cell wall consists from cellulose ($\text{C}_6\text{H}_{10}\text{O}_5$), hemicellulose, lignin ($\text{C}_9\text{H}_{10}\text{O}_2$, $\text{C}_{10}\text{H}_{12}\text{O}_3$, $\text{C}_{11}\text{H}_{14}\text{O}_4$) and pectin ($\text{C}_6\text{H}_{10}\text{O}_7$) and their density is ranging around 1.5 gr/cm^3 (Kellogg & Wangaard, 1969; Gibson, 2012).

Wood, as a porous material, also contains air (N_2 , O_2 , Ar and CO_2) (0.001225 g/cm^3) and water (H_2O) (1 g/cm^3). Thus, it is critical for precise CT density measurements to dry the imaging phantom and the examined wood samples to constant moisture content (Cleaveland, 1983). Phiri (2013) showed how differences in drying temperature can affect the equilibrium weight of Eucalyptus. In X-ray densitometry, the air-dried density (around 12%) is common (Bouriaud et al., 2005; Taylor, 2006; Tomazello et al., 2008; Freyburger et al., 2009; De Ridder et al., 2011). The moisture content of the stem discs and the imaging phantom materials was not measured again after the scans. Thus, the CT density error can possibly be partially attributed to the control of the moisture content.

Furthermore, wood contain various extractives which are organic and inorganic, non-structural materials that contribute to density substantially, especially in heartwood (Cown & Harris, 1991). In particular, conifers are known to have high resin contents and can additionally form pitch pockets (Seifert et al. 2010b). In order for the scanned materials to have similar chemical composition, resins can be removed by alcohol (Zamudio et al., 2002) or an alcohol-benzene solution (Cleaveland, 1983). It is possible that such differences in chemical composition can also be considered partially responsible for the CT density error. In

this point, the densities of CT-scanned samples are not comparable with results from 2D X-ray densitometry, where typically the extractives are extracted before X-ray exposure.

Regarding acetal ((CH₂O)_n), it can be concluded that its different chemical composition had not a significant effect on its grey value, since it lined up visually with the other materials and it increased the coefficient of determination of the regressions. This was expected since acetal is traditionally used as a homogeneous calibration material for 2D X-ray densitometry (e.g. Hoag 1988)

4.1.5. Stability of the calibrations

In studies with medical CT scanners, a single calibration equation is reported to be sufficient, provided the scanner settings are kept the same (Lindgren, 1991a; Taylor, 2006; Freyburger et al., 2009). In contrast, in this study, each reconstructed volume needed a specific greyscale - density calibration equation. This can be attributed to the automatic assignment of the grey values (grey value scaling) by the CT scanner, with black voxels representing air as the material with the lowest density in the scan and white voxels representing poster putty as the material with the highest density in the scan. Specifically, it could be observed by visual inspection of the images that some volumes were brighter or darker than others. Therefore, the shift of the grey values from volume to volume contributed to differences of the calibration equations.

It has to be noted, though, that the shift of the grey values did not affect the CT density error. Specifically, in seven volumes, the whitest voxels belonged to (metallic) staples. Although, the assignment of the grey values was different, the CT density error of these volumes was about the same with the rest.

To sum up these results, it can be stated that it is necessary to scan calibration phantoms with every scan, if a plausible and comparable density should be determined.

4.2. Spatial accuracy

A higher spatial resolution increases the structural detail of a reconstructed object. A higher resolution can be achieved by reducing the distance between the X-ray tube and the object so that and the projection on the detector is covered by more detector elements. Thus, it was attempted to minimize this distance as much as possible. The distance that was chosen as optimal was the distance that the projection of the larger stack of stem discs was marginally

fitting on the X-ray detector. This distance resulted in a spatial resolution of approximately 150 $\mu\text{m}/\text{voxel}$ or 6.7 voxels/mm when scanning a stack of discs.

In comparison with a similar study, De Ridder et al., (2011) scanned wood cores with a spatial resolution of 50 $\mu\text{m}/\text{voxel}$. In X-ray radiography, the spatial resolution (digitized X-ray film negatives) is larger and each ring can be divided in 100 segments in order to provide an equal number of density values (Cleaveland, 1983; Bouriaud et al., 2005; Rathgeber et al., 2006). However the obtainable resolution is clearly determined by sample size which in this study was considerably larger than in the other mentioned studies so that a trade-off between sample size and spatial resolution was evident.

4.3. Outlook on future work

The requirement for accurately-determined CT density and the requirement for comparison of results from different studies that involve CT densitometry lead inevitably to the standardization of the CT densitometry of wood. Thus, future work that targets this standardization could focus on:

- i) The fabrication and use of homogeneous phantom compartments from cellulose of different packing. An alternative to solid wood phantoms can be the use of wood pulp phantoms from wood pulp of various densities. This is similar to the calibration wedges from wood pulp that have been used in X-ray radiography (Cleaveland, 1983). Furthermore, if the chemical composition of a wood pulp phantom was to be known, then the density could be calculated in principle and it could be used as a prediction for the CT density.
- ii) The automatic volume-based grey value measurement of phantom slices in order to increase the accuracy and repeatability of the grey value measurement process. Additionally, the automatic measurement could decrease the required time for measuring a phantom slice and thus it could process a larger number of phantom slices which would increase the accuracy of the calibration and the accuracy of the validation. The automatic measurement possible through the fabrication of the proper phantom and the use of the proper software (Stoel et al., 2008).
- iii) The effect of various factors such as voltage, amperage and effective atomic number on the greyscale - density calibration.

- iv) The simultaneous scan of imaging phantom and wood samples and its effect on the greyscale - density calibration due to artefacts such as beam hardening.
- v) The further investigation of the stability of the calibration procedure with perspective the derivation of a single calibration equation.

With these proposed future improvements, X-ray based microdensitometry could unfold its full potential with regards to the application in wood and forest science.

5. Conclusions

It was successfully demonstrated that an industrial cone-beam CT scanner can be used for wood microdensitometry and, furthermore, for the creation of tree ring CT density profiles.

The absolute CT density error of the reconstructed volumes was ranging from 0.002 - 0.026 g/cm³ with a mean of 0.008 g/cm³ ($\sigma=0.004$) (Figure 15). The percent CT density error of the reconstructed volumes was ranging from 0.4% - 4.4% with a mean of 1.4% ($\sigma=0.7$) (Figure 16).

The CT density error can possibly be attributed to:

- (i) The small number of phantom slices. Specifically, six phantom slices were used for the greyscale - density calibration and three for the validation of the calibration.
- (ii) Differences in the chemical composition of the phantom slices and the wood samples. These are the moisture content, resins and various other extractives.

The CT density error cannot be attributed to the inhomogeneity of wood.

Acetal can be used as an extra reference material in the imaging phantom, since its different chemical composition in relation to wood does not affect its grey value.

Lastly, it is necessary to scan calibration phantoms with every scan, in order to achieve a plausible and comparable density.

6. Reference List

- Beer, A. (1852). Bestimmung der Absorption des rothen Lichts in farbigen Flüssigkeiten (Determination of the absorption of red light in colored liquids). *Annalen der Physik und Chemie*, 86, 78-88.
- Bouriaud, O., Leban, J. M., Bert, D., & Deleuze, C. (2005). Intra-annual variations in climate influence growth and wood density of Norway spruce. 25(6), 651-660.
doi:10.1093/treephys/25.6.651
- Briffa, K. R., Jones, P. D., Osborn, T. J., Schweingruber, F. H., Shiyatov, S. G., & Vaganov, E. A. (2002). Tree-ring width and density data around the Northern Hemisphere: Part 1, local and regional climate signals. *The Holocene*, 12, 737-757.
doi:10.1191/0959683602hl587rp
- Briffa, K. R., Jones, P. D., Schweingruber, F. H., & Osborn, T. J. (1998). Influence of volcanic eruptions on Northern hemisphere summer temperatures over the past 600 years. *Nature*, 393, 450-455.
- Briffa, K. R., Jones, P. D., Schweingruber, F. H., Shiyatov, S. G., & Cook, E. R. (1995). Unusual twentieth-century summer warmth in a 1000-year temperature record from Siberia. *Nature*, 376, 156-159.
- Bucur, V. (2003a). *Non-destructive Characterization and Imaging of Wood* (1st ed.). Berlin: Springer Verlag Berlin Heidelberg New York.
- Bucur, V. (2003b). Ultrasonic imaging of wood structure. *Proceedings of the World Congress on Ultrasonics*. Paris: Société française d'acoustique.
- Chave, J., Muller-Landau, H. C., Baker, T. R., Easdale, T. A., ter Steege, H., & Webb, C. O. (2006). Regional and phylogenetic variation of wood density across 2456 neotropical tree species. *Ecological Applications*, 16(6), 2356-2367.
- Cleaveland, M. K. (1983). *X-Ray Densitometric Measurement of Climatic Influence on the Intra-Annual Characteristics of Southwestern Semiarid Conifer Tree Rings*. PhD Thesis: University of Arizona.
- Cleaveland, M. K. (1986). Climatic Response of Densitometric Properties in Semiarid Site Tree Rings. *Tree-Ring Bulletin*, 46, 13-29.

- Cook, E. R., & Kairiukstis, L. A. (1990). *Methods of Dendrochronology*. Netherlands: Springer. doi:10.1007/978-94-015-7879-0
- Cormack, A. M. (1963). Representation of a function by its line integrals, with some radiological applications. *Journal of applied physics*, 34(9), 2722-2727.
- Cown, D. J. (1999). *Wood Characteristics of New Zealand Radiata pine and Douglas fir: Suitability for processing* (2nd ed.). Rotorua, New Zealand: New Zealand Forestry Corporation Limited.
- Cown, D. J., & Ball, R. D. (2001). Wood densitometry of ten Pinus radiata families at seven contrasting sites: Influence of tree age, site and genotype. *New Zealand Journal of Forest Science*, 31(1), 88-100.
- Cown, D. J., & Harris, J. M. (1991). Basic Wood Properties. In J. A. Kinimonth, & L. J. Whitehouse, *Properties and uses of New Zealand Radiata pine* (Vol. 1, pp. 6.1-6.28). Rotorua, New Zealand: New Zealand Ministry of Forestry, Forest Research Institute, with assistance from the New Zealand Lottery Grants Board.
- Cown, D. J., & McConchie, D. L. (1980). Wood property variations in an old-crop stand of radiata pine. *New Zealand Journal of Forestry Science*, 10(3), 508-520.
- Cown, D. J., McConchie, D. L., & Young, G. D. (1991). *Radiata Pine: Wood Properties Survey*. Rotorua, New Zealand: Forest Research Institute.
- D'Arrigo, R. D., Jacoby, G. C., & Free, R. M. (1992). Tree ring width and maximum latewood density at the North American tree line: parameters of climate change. *Canadian Journal of Forest Research*, 22, 1290-1296.
- De Ridder, M., Van den Bulcke, J., Vansteenkiste, D., Van Loo, D., Dierick, M., Masschaele, B., . . . Van Acker, J. (2011). High-resolution proxies for wood density variations in Terminalia superba. *Annals of Botany*, 107(2), 293-302. doi:10.1093/aob/mcq224
- Decoux, V., Varcin, É., & Leban, J.-M. (2004). Relationships between the intra-ring wood density assessed by X-ray densitometry and optical anatomical measurements in conifers. Consequences for the cell wall apparent density determination. *Annals of Forest Science*, 61, 251-262. doi:10.1051/forest:2004018

- du Plessis, A., Meincken, M., & S. T. (2013). Quantitative Determination of Density and Mass of Polymeric Materials Using Microfocus Computed Tomography. *Journal of Nondestructive Evaluation*, 32, 413–417.
- Espinoza, G. R., Hernández, R., Condal, A., Verret, D., & Beauregard, R. (2005). Exploration of the Physical Properties of Internal Characteristics of Sugar Maple Logs and Relationships with CT Images. *Wood and Fiber Science*, 37(4), 591-604.
- Fischer, P. M. (2011). *$\delta^{13}C$ as indicator of soil water availability and drought stress in *Pinus radiata* stands in South Africa*. Stellenbosch: Stellenbosch University.
- Forest Products Commission Western Australia. (2015). *Forest Products Commission Western Australia*. Retrieved 12 10, 2015, from http://www.fpc.wa.gov.au/content_migration/plantations/species/plantations/radiata_pine.aspx
- Freyburger, C., Longuetaud, F., Mothe, F., Constant, T., & Leban, J.-M. (2009). Measuring wood density by means of X-ray computer tomography. *Annals of Forest Science*, 66(8). doi:<10.1051/forest/2009071>
- Fritts, H. (1976). *Tree Rings and Climate*. London: Academic Press Inc.
- Gibson, L. J. (2012). The hierarchical structure and mechanics of plant materials. *Journal of the Royal Society*.
- Guilley, É., Hervé, J.-C., Huber, F., & Nepveu, G. (1999). Modelling variability of within-ring density components in *Quercus petraea* Liebl. with mixed-effect models and simulating the influence of contrasting silvicultures on wood density. *Annals of Forest Science*, 56, 449-458.
- Hoag, M. L. (1988). *Measurement of Within-Tree Density Variations in Douglas-fir (*Pseudotsuga menzeisii* (Mirb.) Franco Using Direct Scanning X-ray Techniques*. MSc Thesis: Oregon State University p.96.
- Hou, Z. Q., Wei, Q., & Zhang, S. Y. (2007). Predicting density of green logs using the computed tomography technique. *Forest Products Journal*, 59(5), 53-57.
- Hounsfield, G. N. (1973). Computerized transverse axial scanning (tomography): Part 1. Description of system. *The British journal of radiology*, 46(552), 1016-1022.

- Hughes, M. K., Schweingruber, F. H., Cartwright, D., & Kelly, P. M. (1984). July-August temperature at Edinburgh between 1721 and 1975 from tree-ring density and width data. *Nature*, *308*, 341-344.
- Kalender, W. A. (2000). *Computed Tomography*. MCD Verlag.
- Kellogg, R. M., & Wangaard, F. F. (1969). Variation in The Cell-Wall Density of Wood. *Wood and Fiber Science*, *1*.
- Klisz, M. (2013). Genetic control of wood density, tracheid dimension and annual ring traits - an analysis of genetic and phenotypic correlation in European larch. *Annals of Warsaw University of Life Sciences - SGGW*, *83*, 37-41.
- Knapic, S., Louzada, J. L., Leal, S., & Pereira, H. (2007). Radial variation of wood density components and ring width in cork oak trees. *Annals of Forest Science*, *64*(2), 211-218. doi:10.1051/forest:2006105
- Koubaa, A., Zhang, S. T., & Makni, S. (2002). Defining the transition from earlywood to latewood in black spruce based on intra-ring. *Annals of Forest Science*, *59*(5-6), 511-518. doi:10.1051/forest:2002035
- Laufenberg, T. L. (1986). Using gamma radiation to measure density gradients in reconstituted wood products. *Forest Products Journal*, *36*(2), 59-62.
- Lindgren, L. O. (1991a). Medical CAT-scanning X-ray absorption coefficients, CT-numbers and their relation to wood density. *Wood Science Technology*, *25*, 341-349.
- Lindgren, L. O. (1991b). The accuracy of medical CAT-scan images for non-destructive density measurements in small volume elements within solid wood. *Wood Science Technology*, *25*, 425-432.
- Macedo, A., Vaz, C. M., Pereira, J. C., Naime, J. M., Cruvinel, P. E., & Crestana, S. (2002). Wood density determination by X- and gamma-ray tomography. *Holzforschung*, *56*(5), 535-540.
- Magalhães, T. M., & Seifert, T. (2015a). Estimation of tree biomass, carbon stocks and error propagation in Mecrusse woodlands. *Open Journal of Forestry*, *5*, 471-488.

- Magalhães, T. M., & Seifert, T. (2015b). Tree component biomass expansion factors and root-to-shoot ratio of Lebombo ironwood: measurement uncertainty. *Carbon Balance and Management*, 10(9). doi:DOI: 10.1186/s13021-015-0019-4
- Mäkipää, R., & Linkosalo, T. (2011). A Non-Destructive Field Method for Measuring Wood Density of Decaying Logs. *Silva Fennica*, 45(5), 1135–1142. Retrieved from <http://www.metla.fi/silvafennica/full/sf45/sf4551135.pdf>
- Mull, R. T. (1984). Mass Estimates by Computed Tomography: Physical Density from CT Numbers. *American Journal of Roentgenology*, 143, 1101-1104.
- Nikolova, P. S., Blaschke, H., Matyssek, R., Pretzsch, H., & Seifert, T. (2009). Combined application of computer tomography and light microscopy for analysis of conductive xylem area in coarse roots of European beech and Norway spruce. *European Journal of Forest Research*, 128, 145-153. doi:10.1007/s10342-008-0211-0
- Nocetti, Rozenberg, Chaix, & Macchioni. (2011). Provenance effect on the ring structure of teak (*Tectona grandis* L.f.) wood by X-ray microdensitometry. *Annals of Forest Science*, 68(8), 1375-1383. doi:10.1007/s13595-011-0145-4
- Odhiambo, B. O. (2015). *The effect of fire damage on the growth and survival mechanisms of selected native and commercial trees in South Africa. PhD thesis at the Department of Forest and Wood Science.* Stellenbosch University, South Africa.
- Parker, M. L., & Meleskie, K. R. (1970). Preparation of X-ray negatives of tree-ring specimens for dendrochronological analysis. *Tree-Ring Bulletin*, 30, 11-22.
- Phillips, D. H., & Lannutti, J. J. (1997). Measuring physical density with X-ray computed tomography. *NDT&E International*, 30(6), 339-350.
- Phillips, E. W. (1960). The beta ray method of determining the density of wood and the proportion of summerwood. *Journal of the Institute of Wood Science*, 5-8.
- Phiri, D. (2013). *Biomass Modelling of Selected Drought Tolerant Eucalypt Species in South Africa. MSc thesis at the Department of Forest and Wood Science.* Stellenbosch University, South Africa.

- Phiri, D., Ackerman, P. A., Wessels, B., Johansson, M., Säll, H., Lundqvist, S.-O., . . . Seifert, T. (2015). Biomass Equations for Selected Drought Tolerant Eucalypts in South Africa. *Southern Forests*, 3, 1-8. doi:10.2989/20702620.2015.1055542
- Polge, H. (1966). Établissement des courbes de variation de la densité du bois par exploration densitométrique de radiographies d'échantillons prélevés à la tarière sur des arbres vivants : applications dans les domaines Technologique et Physiologique. *Annals of Forest Science*, 23(1), 1-206. doi:10.1051/forest/19660101
- Polge, H. (1970). The use of X-ray densitometric methods in dendrochronology. *Tree-ring bulletin*, 30(1), 1-10.
- Rathgeber, C. B., Decoux, V., & Leban, J.-M. (2006). Linking intra-tree-ring wood density variations and tracheid anatomical characteristics in Douglas fir (*Pseudotsuga menziesii* (Mirb.) Franco). *Annals of Forest Science*, 63(7), 699-706. doi:10.1051/forest:2006050
- Rautkari, L., Kamke, F. A., & Hughes, M. (2010). Potential error in density profile measurements for wood composites. *European Journal of Wood and Wood Products*, 69(1), 167-169. doi:10.1007/s00107-010-0419-9
- Revel, R. (1982). The use of scanning electron microscopy as a tool in dendrochronology. *Tree-Ring Bulletin*, 42, 57-64.
- Rinn, F. (2012). Basics of typical resistance-drilling profiles. *Western Arborist*, 30-36.
- Rinn, F., Schweingruber, F. H., & Schär, E. (1996). RESISTOGRAPH and X-ray Density Charts of Wood Comparative Evaluation of Drill Resistance Profiles and X-ray Density Charts of Different Wood Species. *Holzforschung*, 50(4), 303-311.
- Robinson, A. P., & Hamann, J. D. (2011). *Forest Analytics with R*. New York, Dordrecht, Heidelberg, London: Springer Science+Business Media. doi:10.1007/978-1-4419-7762-5
- Schinker, M. G., Hansen, N., & Spiecker, H. (2003). High-Frequency Densitometry – A New Method for the Rapid Evaluation of Wood Density Variations. *IAWA Journal*, 24(3), 231-239.

- Schweingruber, F. H. (1988). *Tree Rings: Basics and Applications of Dendrochronology*. (1, Ed.) Dordrecht: Springer Netherlands. doi:10.1007/978-94-009-1273-1
- Schweingruber, F. H., & Kienast, F. (1986). Dendroecological Studies in the Front Range, Colorado, U.S.A. *Arctic and Alpine Research*, 18(3), 277-288. Retrieved from <http://www.jstor.org/stable/1550885>
- Schweingruber, F., Fritts, H., Bräker, O., Drew, L., & Schär, E. (1978). The X-Ray Technique as Applied to Dendroclimatology. *Tree-Ring Bulletin*, 38, 61-91.
- Seifert, T., & Seifert, S. (2014). Modelling and simulation of tree biomass. In T. Seifert (Ed.), *Bioenergy from Wood: Sustainable Production in the Tropics* (1 ed., pp. 42-65). Netherlands: Springer.
- Seifert, T., Breibeck, J., Seifert, S., & Biber, P. (2010b). Resin pocket occurrence in Norway spruce depending on tree and climate variables. *Forest Ecology and Management*, 260, 302–312.
- Seifert, T., Nickel, M., & Pretzsch, H. (2010). Analysing the long-term effects of artificial pruning of wild cherry by computer tomography. *Trees*, 24, 797-808. doi:10.1007/s00468-010-0450-9
- Steppe, K., Cnudde, V., Girard, C., Lemeur, R., Cnudde, J.-P., & Jacobs, P. (2004). Use of X-ray computed microtomography for non-invasive determination of wood anatomical characteristics. *Journal of Structural Biology*, 148, 11-21. doi:10.1016/j.jsb.2004.05.001
- Stoel, B. C., Bode, F., Rames, A., Soliman, S., Reiber, J. H., & Stolk, J. (2008, 12 15). Quality Control in Longitudinal Studies with Computed Tomographic Densitometry of the Lungs. *Proceedings of the American Thoracic Society*, 5(9), 929-933.
- Taylor, A. J. (2006). *Wood density determination in Picea sitchensis using computerised tomography; how do density measurements compare with measurements of pilodyn pin penetration (Honours Project)*. Bangor: The University of Wales.
- Tomazello, M., Brazolin, S., Chagas, M. P., Oliveira, J. T., Ballarin, A. W., & Benjamin, C. A. (2008). Application of X-Ray Technique in Nondestructive Evaluation of Eucalypt Wood. *Maderas: Ciencia y tecnología*, 10(2), 139-149.

- Vaganov, E. A., Hughes, M. K., & Shashkin, A. V. (2006). *Growth Dynamics of Conifer Tree Rings*. Berlin Heidelberg: Springer-Verlag.
- Vahey, D. W., Zhu, J. Y., & Scott, C. T. (2007). Wood density and anatomical properties in suppressed-growth trees: Comparison of two methods. *Wood and Fiber Science*, 39(3), 462-471.
- Warton, D., Wright, I., Falster, D., & Westoby, M. (2006). Bivariate line-fitting methods for allometry. *Biological reviews of the Cambridge Philosophical Society*, 81(2), 259–291.
- Wessels, C. B., Malan, F. S., Seifert, T., Louw, J. H., & Rypstra, T. (2015). The prediction of the flexural lumber properties from standing South African grown *Pinus patula* trees. *European Journal of Forest Research*, 134(1), 1-18.
- Zamudio, F., Baettyg, R., Vergara, A., Guerra, F., & Rozenberg, P. (2002). Genetic trends in wood density and radial growth with cambial age in a radiata pine progeny test. *Annals of Forest Science*, 59(5-6), 541-549. doi:10.1051/forest:2002039
- zu Castell, W., Schrödl, S., & Seifert, T. (2005). Volume Interpolation of CT Images from Tree Trunks. *Plant Biology*, 7, 737-744.

Appendix A. Regression example

The regression dataset was saved as an 'xlsx' file (Table 6). The first column has the conventionally-determined density of the phantom slices and the second column has the grey value of the phantom slices of a reconstructed volume.

Table 6 - Example of a regression dataset

Convotional_density	gv_volume1
0.209	44.99155
0.407	59.32669
0.546	70.9091
0.82	92.31391
0.901	98.98724
1.248	124.36734

The following code was written in R. It requires the packages lmodel2 and Rcmdr.

Load the required packages

library(lmodel2)

library(Rcmdr)

#Go to R commander, click on "Data->Import data->from Excel, Access, dBase data set...", name the data "dataset" on the pop-up window and then browse to the 'xlsx' file that has the regression dataset.

Load the columns of the table into variables

Convotional_density = Dataset\$Convotional_density

gv_volume1 = Dataset\$gv_volume1

Do the regressions

Regression_volume1 <-lmodel2(Convotional_density~ gv_volume1, data=Dataset, "interval", "interval",99)

Print the regression results

Regression_volume1

The following are part of the regression results:

> Regression_volume1

Model II regression

R² = 0.9998112

Parametric P-value (1-tailed) = 6.687474e-09

Regression results

<i>Method</i>	<i>Intercept</i>	<i>Slope</i>	<i>Angle (degrees)</i>	<i>P-perm (1-tailed)</i>
<i>RMA</i>	<i>-0.3847041</i>	<i>0.01309576</i>	<i>0.7502888</i>	<i>0.01</i>

Appendix B. Regression results

Table 7 - The equations and the coefficients of determination of the regressions

Reconstructed volume	Greyscale - density calibration equation	Coefficient of determination (R ²)
1	CT density = 0.01148161* gv - 0.3321912	>99.9%
2	CT density = 0.007370822* gv - 0.3101589	>99.9%
3	CT density = 0.01330115* gv - 0.3809996	>99.9%
4	CT density = 0.01264336* gv - 0.2817903	>99.9%
5	CT density = 0.007753436* gv - 0.3802119	>99.9%
6	CT density = 0.01309576* gv - 0.3847041	>99.9%
7	CT density = 0.03721415* gv - 0.6603485	>99.9%
8	CT density = 0.01294966* gv - 0.3149188	>99.9%
9	CT density = 0.01318806* gv - 0.355699	>99.9%
10	CT density = 0.01156662* gv - 0.3905499	>99.9%
11	CT density = 0.01277104* gv - 0.3096305	>99.9%
12	CT density = 0.01365867* gv - 0.3173754	99.9%
13	CT density = 0.007542727* gv - 0.3255008	99.9%
14	CT density = 0.01166322* gv - 0.3129883	99.9%
15	CT density = 0.01263453* gv - 0.361692	99.9%
16	CT density = 0.01225891* gv - 0.4121855	99.9%
17	CT density = 0.0123316* gv - 0.2845394	99.9%
18	CT density = 0.01316043* gv - 0.3456086	99.9%
19	CT density = 0.007525346* gv - 0.3234818	99.9%
20	CT density = 0.01235991* gv - 0.351937	99.9%
21	CT density = 0.01207482* gv - 0.3793724	99.8%
22	CT density = 0.01412469* gv - 0.459653	99.8%
23	CT density = 0.01308913* gv - 0.4052635	99.8%
24	CT density = 0.01237483* gv - 0.3183946	99.8%
25	CT density = 0.01157408* gv - 0.3069922	99.8%
26	CT density = 0.01151418* gv - 0.5131545	99.8%
27	CT density = 0.01319592* gv - 0.2893366	99.8%
28	CT density = 0.0133217* gv - 0.3950061	99.8%
29	CT density = 0.01373134* gv - 0.3482365	99.8%
30	CT density = 0.01685997* gv - 0.5263209	99.8%
31	CT density = 0.01274244* gv - 0.3349409	99.8%
32	CT density = 0.01331264* gv - 0.3364057	99.8%
33	CT density = 0.013784* gv - 0.3544914	99.8%
34	CT density = 0.0127086* gv - 0.3740552	99.8%
35	CT density = 0.01676673* gv - 0.5163949	99.8%
36	CT density = 0.01364231* gv - 0.3469475	99.8%
37	CT density = 0.01308079* gv - 0.3788067	99.8%
38	CT density = 0.01328738* gv - 0.5540642	99.8%
39	CT density = 0.01308768* gv - 0.361368	99.8%

40	CT density = 0.01489911* gv - 0.5230056	99.7%
41	CT density = 0.01433946* gv - 0.5391068	99.7%
42	CT density = 0.01278225* gv - 0.3189747	99.7%
43	CT density = 0.01316803* gv - 0.3365204	99.7%
44	CT density = 0.01380651* gv - 0.3591638	99.7%
45	CT density = 0.01251666* gv - 0.3698284	99.6%
46	CT density = 0.012208* gv - 0.4742786	99.5%
47	CT density = 0.01311183* gv - 0.3332879	99.5%
48	CT density = 0.01205683* gv - 0.5837271	99.5%
49	CT density = 0.01345658* gv - 0.320354	99.3%
50	CT density = 0.008114646* gv - 0.4188082	99.0%
